Hyperspectral Vibrational Imaging of Tumor Tissue

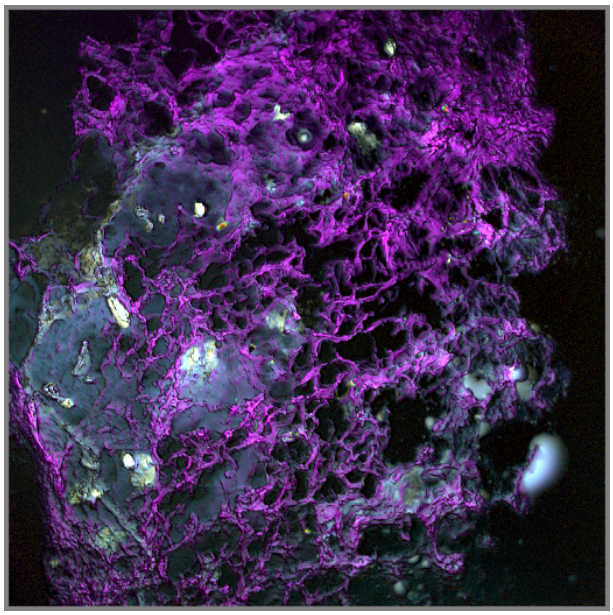

Master Thesis
Applied Physics
Optical Sciences, Faculty TNW
University of Twente

March 26, 2015

Author:
Sven A. van Binsbergen

Committee:
Prof. dr. Jennifer L. Herek
Dr. Herman L. Offerhaus
Dr. Christian Blum

Abstract

Presented here is the research done in course of a Master's assignment for Applied Physics, in the Optical Sciences research group at the University of Twente.

Raman spectroscopy is a technique used in a wide variety of research fields including cancer research. By probing the vibrational resonances of tissue in both the specific fingerprint region as well as the stronger but more general high wavenumber region, spectral differences between healthy and cancerous tissue can be detected. While accurate, it is a very slow method. An alternative called CARS, Coherent anti-Stokes Raman Scattering, yields results much faster but suffers from a strong non-resonant background that deforms the original Raman spectrum.

This research aims to evaluate the possible use of CARS spectroscopy to distinguish cancer tissue from healthy tissue. The non-resonant background is largely dealt with by applying a modified Kramers-Kronig algorithm that isolates the resonant signal from the background. Results were very promising in the high wavenumber region while the SNR in the fingerprint region was too low for successful extraction of useful data. The retrieved spectra are displayed using a hyperspectral imaging scheme that displays more information than a standard 3-channel RGB image.

In the high wavenumber region, spectral differences within tissue samples were easily shown in many results. We were unable to show that differences between healthy and cancer tissue could be detected as well due to difficulties locating tumor areas in order to perform comparative measurements.

Nonetheless, we are confident that CARS can be used to distinguish tumors from healthy tissue in the high wavenumber region. With some adjustments and improvements useful operation is also expected in the fingerprint region. Recommendations for a successful continuation of the project are provided.

Uittreksel

In dit schrijven wordt verslag gedaan van het onderzoek verricht in de vorm van een afstudeeropdracht voor de master Applied Physics bij de vakgroep Optical Sciences aan de Universiteit Twente.

Raman spectroscopie is een techniek die wijdverspreid is in verschillende onderzoeksrichtingen, waaronder kankeronderzoek. Door vibrationele resonanties van weefsel in zowel de specifieke fingerprint region als ook in de sterkere maar algemenere high wavenumber region te detecteren kunnen spectrale verschillen tussen gezond weefsel en kankerweefsel herkend worden. Hoewel dit een nauwkeurige methode is, is zij ook erg traag. Een alternatief genaamd CARS - Coherent anti-Stokes Raman Scattering - is veel sneller maar heeft last van een sterk niet-resonant achtergrondsignaal dat het oorspronkelijke Ramanspectrum vervormt.

Dit onderzoek werpt een blik op de mogelijkheid om CARS spectroscopie te gebruiken om gezond en kankerweefsel van elkaar te onderscheiden. Het niet-resonante achtergrondsignaal wordt grotendeels geneutraliseerd door een aangepaste Kramers-Kronig relatie te gebruiken die het resonante deel van het achtergrondsignaal isoleert. In de high wavenumber region leverde dit veelbelovende resultaten, in de fingerprint region was de signaal-ruisverhouding te laag voor een successvolle verwerking. De geïsoleerde spectra werden vervolgens door middel van een hyperspectrale afbeeldingsmethode afgebeeld.

In de high wavenumber region waren spectrale verschillen binnen weefselmonsters duidelijk zichtbaar. Het bleek erg lastig om voor de CARS-metingen de locatie van het tumorweefsel vast te stellen, waardoor vergelijkende metingen tussen gezond en kankerweefsel bemoeilijkt werden. Hierdoor is het niet gelukt direct verschil tussen gezond en kankerweefsel zichtbaar te maken.

Niettemin zijn we ervan overtuigd dat CARS gebruikt kan worden om kankerweefsel van gezond weefsel te kunnen onderscheiden in de high wavenumber region. Met een aantal aanpassingen en verbeteringen verwachten wij dat dit ook in de fingerprint region mogelijk zal zijn. Tot slot wordt een aantal mogelijke vervolgstappen voor dit onderzoek genoemd.

Contents

1 Introduction **2**
- 1.1 Motivation . . . 2
- 1.2 Outline of this report . . . 3

2 Raman scattering and spectroscopy **5**

3 Raman spectroscopy on cancer tissue **8**

4 Stimulated Vibrational Resonances **11**
- 4.1 CARS . . . 11
- 4.2 SRS . . . 13

5 Setup **15**
- 5.1 CARS Setup . . . 15
- 5.2 SRS Setup . . . 17

6 Sample preparation **18**
- 6.1 Initial samples . . . 18
- 6.2 Main samples . . . 19
- 6.3 FISH & DAPI staining . . . 20

7 Data Processing **21**
- 7.1 Hyperspectral imaging . . . 21
- 7.2 Extracting a Raman signal . . . 24

8 Results **28**
- 8.1 First results with Kramers-Kronig . . . 28
- 8.2 Fingerprint attempts . . . 31
- 8.3 Cryomatrix effects . . . 34
- 8.4 SRS comparisons . . . 36
- 8.5 Final tissue samples . . . 40

9 Conclusion **49**
- 9.1 Outlook . . . 50

10 Acknowledgements **51**

11 Bibliography **53**

12 Appendix **56**

Chapter 1

Introduction

1.1 Motivation

Each year, over 40,000 people in the Netherlands die of cancer, making it the number one cause for death [1]. Researchers looking for ways to reduce this number can be roughly divided in three groups: those who look for ways to prevent cancer, those who try to diagnose it and those who try to cure it. Researchers in the last two groups benefit greatly from methods that can accurately pinpoint tumor tissue. While blood tests or symptoms are usually sufficient to conclude that something is wrong, more accurate methods are required in order to perform targeted treatments. These methods include for example X-ray scans and MRI imaging [2] for body-wide scans or tissue extraction for analysis in the lab. In some cases fluorescent tagging [3] is also used to indicate surface tumors during an operation.

The problem with the mentioned methods is that many have (medical) drawbacks. X-ray imaging may be able to scan your body part very fast, but the X-rays themselves are - ironically - a risk factor in developing new tumors [4]. Fluorescently tagged particles can locate tumors very precisely because they connect to cancer-specific proteins, but here too the markers themselves can be considered to be carcinogenic [4]. Although MRI scans have no obvious medical drawbacks their initial costs and operating costs are immense.

As a result, research on (safer) label-free imaging methods is a strong area. As the name suggests, label-free methods do not require the application of other substances or labels, and work solely by imaging *what is already there*. As such, X-ray imaging could be considered to be label-free, but it still suffers from the use of harmful radiation. The ultimate goal is to find a method where all imaging can be done using methods that don't require anything to be injected into the body (or sample, in case of research), nor harmful radiation to be used, for a reasonable price.

Of course, label-free methods are also of great use for ex vivo research: virtually no sample preparation is required. This reduces the risks of mistakes as well as false signals because of chemicals used during processing. Furthermore, measurements can be performed immediately after extraction of the sample instead of having to wait for preparation procedures to be finished. There is hope that ultimately, safe label-free methods to detect tumors can also be used in vivo. Then, it would even be possible to start safe periodical precautionary scans, since the screening will have no lasting effects.

One of the possible label-free imaging methods is Raman spectroscopy. Being around since the late 1920's [5], it is based on probing the vibrational resonance frequencies of molecules

using narrowband optical excitation. These resonances are directly linked to intramolecular bonds. When the resonances of specific (types of) bonds are known, acquired resonance spectra can be used to identify the (type of) molecules. Since healthy and cancerous tissue have strong differences in their molecular composition, they will generate different Raman spectra[1]. This makes Raman spectroscopy a good label-free method to investigate biological samples.

Although Raman spectroscopy is a very accurate method, it is also very slow due to its inherent inefficiency. While this is acceptable if only a single measurement is required, medical *imaging* typically requires hundreds to hundreds of thousands of datapoints for a simple image: one for every pixel. Alternative techniques involving stimulated emission of Raman scattering such as Coherent anti-Stokes Raman Scattering (CARS) and Stimulated Raman Scattering (SRS) can yield results much faster and are thus much more suitable for imaging. While these methods typically probe only one vibration at a time instead of a whole spectrum, a scan over multiple vibrations is still many times faster than a regular Raman measurement. (Of course, there are varieties such as broadband CARS which can probe broad spectra at once, but these usually lack in other aspects.)

Having access to a full spectrum for each spatial pixel, hyperspectral images can be created, which contain much more information than a regular grayscale or even RGB image.

The goal of this thesis is to use hyperspectral CARS - with SRS in a supporting role - to look into the possible use of CARS microscopy to locate tumor tissue in both cancer diagnosis as well as in a research setting.

It is a part of a larger collaboration between the University Medical Center in Groningen and the University of Twente on cancer research, combining (bio)medical knowledge from Groningen with the physics and imaging-related knowledge from Enschede. The work reported on in this thesis was conducted at the Optical Sciences (OS) research group at the University of Twente, with material and intellectual assistance from the MCBP and DBE groups in Enschede and the departments of Gastroenterology and Hepatology and Medical Oncology at the UMCG.

1.2 Outline of this report

This report aims to provide a clear overview of the work done over the last year on the hyperspectral vibrational imaging of cancer tissue.

Chapter 2 starts out with the fundamentals of Raman Scattering, a phenomenon widely used in vibrational spectroscopy and very useful for distinguishing different molecules in samples.

Chapter 3 will then give a brief overview of previous research done on cancer tissues using Raman spectra. It will focus mostly on the typical spectral features that are known to be present in either or both healthy and tumorous tissue.

Chapter 4 continues where chapter 2 ended by expanding to both Coherent anti-Stokes Raman Scattering (CARS) and Stimulated Raman Scattering (SRS), two stimulated varieties of Raman scattering, each with their own advantages and disadvantages.

[1] See chapter 3 for more information

In chapter 5, the setup is described.

The preparation of the samples provided is discussed in chapter 6. This was done partly in cooperation with other research groups at the University of Twente due to their experience in this field.

Since the raw data gathered by the setup is not yet ready for interpretation, chapter 7 deals with the data processing steps.

Chapters 8 and 9 contain the results and conclusion, respectively. A small outlook to possible future research is also provided at the end of the conclusion.

At the back of this thesis, an appendix can be found containing the postprocessing script used as well as full size prints of the DAPI and FISH scans.

Chapter 2

Raman scattering and spectroscopy

As stated in the introduction, Raman spectroscopy measures the vibrational resonances of molecules. It uses the process of Raman scattering to determine the amount of energy that is transferred from an incident light wave to the molecular vibrations of the sample.

To explain Raman scattering, it is best to start with the most basic form of scattering: Rayleigh scattering. Assuming a monochromatic source such as a laser, a light beam with pump frequency ω_p is incident on the sample, in this case a single molecule. The amount of energy in the photons is such that it doesn't match any electronic or vibrational energy levels of the molecule. As a result, the molecule reaches a short-lived virtual state. In this virtual state, the electron cloud oscillates with the EM-field of the beam while the atoms themselves remain inactive. Shortly after, the molecule falls back to its ground state, releasing the energy in the form of new photons with the same frequency ω_p but in a different direction. This elastic scattering is the principle of Rayleigh scattering.

In isolated cases, the molecule does not directly return to its ground state but drops down to a vibrational state instead. Since part of the energy is now 'taken' by the molecular vibration, the photons that are emitted are of a lower frequency than those that were absorbed. These photons, also called Stokes photons, have frequency ω_s (See figure 2.1). In general, this process happens only once every 10^7 scattering events [6], and thus is very inefficient. This is the principle of Raman scattering.

Of course, due to temperature effects or previous excitation, there is a chance that the molecule is already in a vibrational state when a photon strikes. In this case, the virtual level that is reached due to absorption of the photon will be higher than in the case of Stokes scattering. Thus, when this molecule falls back to its ground state, the emitted photons will have a higher frequency ω_{as}. In most situations, these anti-Stokes photons are even rarer than Stokes photons due to the low amount of pre-excited molecules. Their advantage however is that they can be easier to detect than the lower-frequency Stokes photons since they don't have to compete with other lower-frequency signals such as autofluorescence.

While Stokes and anti-Stokes photons have been theoretically suggested by Adolf Smekal in 1923 [7], it took 5 more years until Chandrasekhara Venkata Raman observed them in his lab [5].

Observing the difference frequency of the pump and (anti-)Stokes photons is the essence

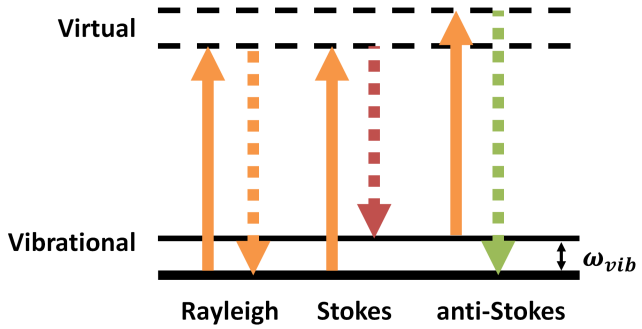

Figure 2.1: Rayleigh scattering and Raman scattering, with Stokes and anti-Stokes photons.

of Raman spectroscopy. These values are the resonance frequencies of the vibrational levels, which are typical for specific molecules. A molecule can be compared to a complex mass-spring system, where the atoms are the masses while the intramolecular bonds are the springs. Variations in mass and bond stiffness will result in different resonance frequencies. Thus, after creating a database of known resonances, one can link certain vibrational resonances to specific (types of) molecules.

The schematic energy diagram shown in figure 2.1 might suggest that all vibrational resonances can be probed using Raman scattering, but these transitions are restricted by selection rules. In fact, Raman spectroscopy can be combined with IR spectroscopy to extract more vibrational information that is unavailable to Raman spectroscopy itself and vice versa. Where in Raman spectroscopy the vibration of interest is probed by comparing the frequency of the pump and Stokes photons, IR spectroscopy directly excites these resonances. In this case, the energy is absorbed into the vibration, and thus measuring the difference in power going in and coming out of the sample yields an absorption value. By varying the frequency of the incident beam, the absorption can be measured over a broad spectrum as well, resulting in an IR spectrum.

The difference between Raman and IR spectroscopy is not only found in their method of excitation, but also in *what* resonances they can detect. This is strongly related to the effect of the light on the dipole moment (p) and polarizability (α) of the molecule being probed. Vibrations that induce a change in polarizability, but none in the dipole moment, typically have a strong peak in the Raman spectrum but none in the IR spectrum. Many symmetric vibrations have these characteristics. Similarly, vibrations that induce a change in the dipole moment, but none in the polarizability, cause a strong peak in the IR spectrum but none in the Raman spectrum. These characteristics are typical for asymmetric vibrations. Figure 2.2 illustrates an example for both situations.

Although physicists advocate the use of SI units, there are a few examples where tradition beats system. This is also the case for Raman scattering where the vibrational frequency is indirectly provided by using inverse centimeters (cm^{-1}). Even this unit could be considered to be wrong, since Raman scattering is all about the energy difference between the incident pump photons and the scattered Stokes photons. ($\omega_p - \omega_{stokes} = \omega_{vib}$.) Thus, the unit $\Delta\mathrm{cm}^{-1}$, where

$$\Delta\omega(\mathrm{cm}^{-1}) = \left(\frac{1}{\lambda_s(\mathrm{nm})} - \frac{1}{\lambda_p(\mathrm{nm})}\right) \times 10^7 \frac{(\mathrm{nm})}{(\mathrm{cm})} \tag{2.1}$$

would be a more accurate description. However, to adapt to the majority of all papers, I will also continue using cm^{-1} where the Δ is implied.

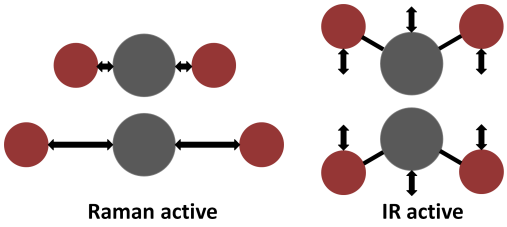

Figure 2.2: Vibrations of a CO_2 molecule. The symmetric Raman active vibration causes a change in the polarizability, while the asymmetric IR active vibration causes a change in the dipole moment of the molecule.

A typical Raman or IR spectrum spans from 100-200 cm^{-1} (50 cm^{-1} for expensive systems [6]) to up to 4000 cm^{-1}. For many samples, this spectrum splits into three regions. (See figure 2.3) The first spans from 200-1850 cm^{-1} and is called the fingerprint region. Many organic molecules have specific (combinations of) peaks in this region, making identification relatively easy. The second region spans from about 1850-2700 cm^{-1}. Here, very few vibrations are available and this region is aptly named the silent region. The final region spans from 2700-4000 cm^{-1}, and is called the high wavenumber region. Here, proteins and fat molecules have typical wide, overlapping peaks and vibrations in water molecules themselves cause one more broad peak.

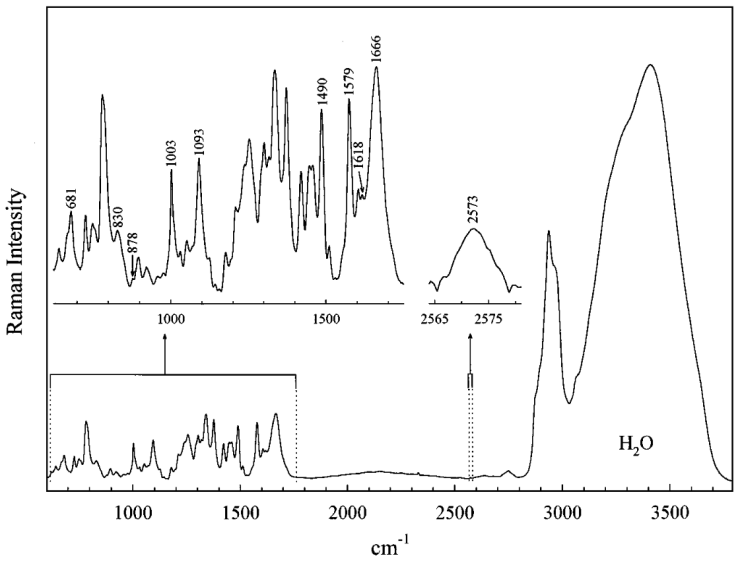

Figure 2.3: Raman spectrum of a P22 virus by [8]. Clearly visible are the weaker fingerprint region on the left, the empty silent region in the middle and the strong high wavenumber region on the right. The high wavenumber region contains signals from protein and lipid vibrations around 2950 cm^{-1} and a very broad water-related resonance at higher wavenumbers.

With its ability to detect vibrational resonances, Raman spectroscopy has found many uses in many different areas. Examples include, but are not limited to temperature measurements [9], gas analysis [10], materials science [11], biological characterisation of bacteria [12], pigment characterization in old paintings [13] and of course many fields of cancer research.

Chapter 3

Raman spectroscopy on cancer tissue

In general, people speak of the disease cancer as if it were one specific disease. However, cancer should perhaps better be considered to be a collective term for many illnesses [14] since different types of cancer can have different causes and exhibit completely different symptoms. As a result, there is no single detection method, and no single cure for all cancer types. Instead, cures need to be specifically tailored to have an effect on the cancer and not on the healthy tissue. Similarly, detection methods might work for one type, but not for another.

The common factor in most cancers is some form of damage to the DNA of the cells. Often, damage to the DNA is repaired by the cell itself, but sometimes this fails, for example when the genes coding for repair are the ones that are damaged. In itself, this still is no problem, since this damaged cell will die without consequences. However, if this damage is combined with more damage, for example in the DNA code regulating cell division, there is a chance that this damaged cell will start - and keep - reproducing at high rates, using up all resources and hindering nearby healthy cells from functioning correctly. These growths of cancer cells are called tumors.

Raman spectroscopy research on cancer aims to measure the Raman spectra of the affected tissues to find spectral characteristics that are typical for cancer. Due to the inhomogeneous nature of cancer types, however, it is difficult to find characteristics that are applicable to all cancers. Looking at the amount of different research projects on all kinds of cancer, one can see quickly that no spectra look really similar. As a result, there are many separate Raman studies for different kinds of cancers. Raman spectroscopy on breast cancer [15], lung cancer [16] and cervical cancer [17, 18] are just a few examples.

Looking at some of the spectra obtained in the research projects mentioned above, both the usefulness and disadvantages of Raman spectroscopy can be seen. For example, in one paper researching breast cancer [15], spectra are shown for healthy and diseased breast tissue (see figure 3.1). In the fingerprint region, two peaks related to caroten content can be noticed to have completely disappeared in cancerous breast tissue. This can be a very strong marker in separating healthy from diseased tissue when looking at breasts specifically, but will be useless when looking at for example ovarian cancer (figure 3.2), since here these intense peaks are absent both for healthy and diseased tissue [19].

Even worse, comparing various papers on similar tissue - such as [17] and [18] - shows that

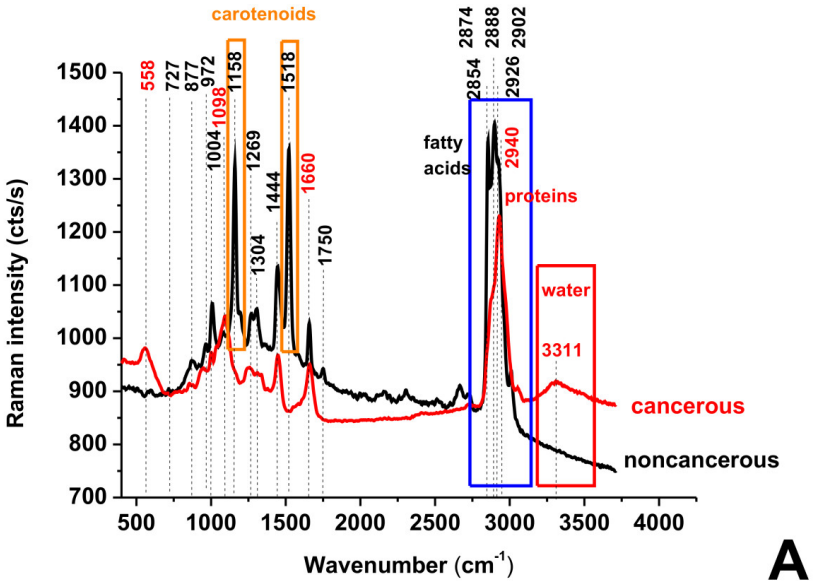

Figure 3.1: Selection from Figure 3 from [15]. Peaks corresponding to carotenoid content at 1158 cm^{-1} and 1518 cm^{-1} have completely disappeared in cancerous tissue.

the spectrum for similar cancers appears to be different in different papers. As such, defining a (change in a) certain peak to be related to cancer can be a difficult task. A cause for this can range from different lifestyles of the sample donors to differences in the preparation of the sample. Fixating the samples in for example paraffin causes new bonds to be formed due to the use of formalin [20] while the paraffin itself also has a strong spectrum.

In general, a common factor between documented cancer spectra is that the protein content in cancer tissue appears to be higher than that of healthy tissue. For lipid content the results vary with clearly less lipids in brain tumors but higher content for example melanoma. The main samples that have been used in this project were of a lung cancer cell line. For lung cancer, the amount of lipids generally decreases in cancer tissue. This behavior could be explained by the continuous replication of cells which requires a lot of energy, resulting in a lower fat reserve. Similarly, the increase of production is facilitated by a larger amount of proteins.

While also available in the fingerprint region, proteins have very strong vibrations at 2930 cm^{-1} and 2980 cm^{-1}, caused by asymmetric CH_3 vibrations. Lipids yield very strong resonances around 2850 cm^{-1} and 2885 cm^{-1} due to symmetric and anti-symmetric stretching of CH_2 groups [21], which are abundant in the long tails of fatty molecules.

The variety in spectra difference clearly shows that it is very useful to measure full spectra instead of just a few specific peaks so that any small differences can be picked up.

Ultimately, this yields two interesting Raman regions to consider: On one hand the fingerprint region with its distinct but weaker peaks and on the other hand the high wavenumber region, with stronger but broader peaks for lipids and proteins.

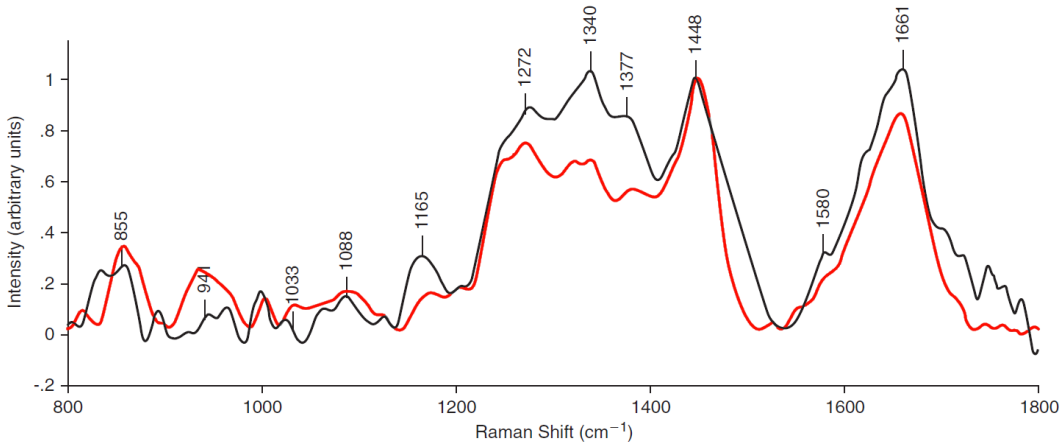

Figure 3.2: Figure taken from [19], colors changed by author for clarity. Shown are the Raman spectra of healthy (red) and cancerous (black) ovarian tissue. The peak at 1661 cm^{-1} is attributed to lipids, the peak at 1448 cm^{-1} to both lipids and proteins.

Chapter 4

Stimulated Vibrational Resonances

While Raman spectroscopy can be a very accurate and useful method, it has one major drawback: speed. Since so few photons participate in Raman scattering, long integration times are required to obtain a decent spectrum. While this might be acceptable for a single point measurement, it usually is not when trying to image (large) samples with high resolution. Even an image of 512*512 pixels, which many people would consider to be 'low resolution' nowadays, still contains about 250.000 pixels. Even when a single spectrum only takes a fraction of a second, a complete Raman scan will easily take hours. Fortunately, there are several other methods related to Raman scattering which can perform measurements much faster - but each with their own drawbacks. Two of them will be discussed in the following chapter.

4.1 CARS

CARS stands for **C**oherent **a**nti-Stokes **R**aman **S**cattering. As the name suggests, it collects the coherent Anti-Stokes photons. Readers who remember chapter 2 on spontaneous Raman scattering might wonder why, since the anti-Stokes beam is a lot weaker than the Stokes beam. To understand this, a bit more physics is required.

In the Raman chapter, the polarizability of the material was already briefly touched upon: When the incident light induces a change in polarization, one can expect Raman scattering. The polarization can be given by

$$P(t) = \epsilon_0 \chi^{(1)} E(t) \tag{4.1}$$

where $P(t)$ is the polarization, $E(t)$ is the electric field (due to the incident light), ϵ_0 is the electric permittivity and $\chi^{(1)}$ is the linear susceptibility which depends on both the material as well as the frequency of the electric field. This equation however is only valid for low power levels that are present in every day life. At higher power levels, higher order terms should be taken into account. A new, or rather "more complete", equation for polarization should thus be:

$$P(t) = \epsilon_0(\chi^{(1)} E(t) + \chi^{(2)} E^2(t) + \chi^{(3)} E^3(t) + ...) \tag{4.2}$$

$\chi^{(2)}$ and $\chi^{(3)}$ are the second and third order nonlinear susceptibility respectively. Only at higher laser powers do their terms become strong enough to be noticed in the total polarization. The second term is often 0, except for non-centrosymmetric cases such as various crystals and asymmetric molecules. SHG (Second Harmonic Generation) and SFG (Sum

Frequency Generation) only occur when $\chi^{(2)}$ is non-zero, but these processes are not important for the rest of this thesis.

$\chi^{(3)}$ Is significant in almost all materials and provides the basis for - among others - THG (Third Harmonic Generation), the optical Kerr effect, cross-phase modulation and FWM (Four Wave Mixing) [22]. CARS is a four wave mixing process.

In Raman spectroscopy, one provides a pump beam and measures the (anti-)Stokes beam. In CARS however, the Stokes beam is provided as well. Since CARS setups usually use high powered pulsed lasers, those beams have to be overlapped not only spatially but also temporally. The interaction between those two beams, where the pump beam provides two photons for every Stokes photon, results in a fourth beam: the anti-Stokes beam. (See figure 4.1 for the schematic.)

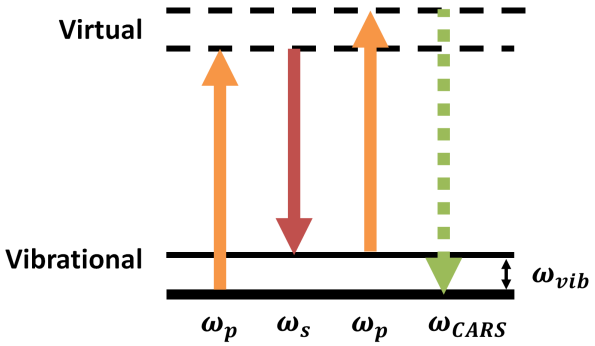

Figure 4.1: Schematic energy diagram showing the principles of CARS.

Looking at the transitions in this scheme, one can understand that

$$I_{CARS} \propto I_{pump}^2 I_{stokes} \tag{4.3}$$

When both the pump beam and the stokes beam are focussed tightly into the sample, the majority of the signal will originate from this focal point. As a result, CARS is not only fast, but also suitable for 3D sectioning, since the focal point can easily be moved around using a galvanometric mirror set in the setup and/or a motorized sample stage in the microscope. Equation 4.3 is also the reason for the use of pulsed lasers: the pulses are of high power resulting in strong signals, while the average laser power remains at acceptable levels, preventing sample damage.

The third order polarization $P^{(3)}$ increases strongly when the difference frequency between the pump and Stokes beams matches a vibrational resonance. This is because $\chi^{(3)}$ is large at those resonances.

$$P^{(3)}(\omega_p, \omega_s; \omega_{as}) = \chi^{(3)}(\omega_p - \omega_s) E_p^2(\omega_p) E_s(\omega_s) \tag{4.4}$$

In most CARS setups, one measures the intensity of the anti-Stokes beam. This intensity scales with the square modulus of the nonlinear susceptibility. Since the nonlinear susceptibility consists of a resonant as well as a non-resonant part, one can write:

$$\begin{aligned} I_{CARS}(\omega) &\propto |\chi^{(3)}(\omega)|^2 \\ &= |\chi_r^{(3)}(\omega) + \chi_{nr}^{(3)}(\omega)|^2 \\ &= |\chi_r^{(3)}(\omega)|^2 + |\chi_{nr}^{(3)}|^2 + 2\chi_{nr}^{(3)} \mathrm{Re}[\chi_r^{(3)}(\omega)] \end{aligned} \tag{4.5}$$

Here, one can see one of the main problems of the CARS technique: the non-resonant component of the susceptibility. In the final term of equation 4.5, we can see this term is squared, just like the resonant component. In areas where there are many sources for a non-resonant signal and only one for a weak resonance, the resonant signal drowns in the non-resonant signal. On top of this, the third term shows a mixing effect where the non-resonant signal coherently adds to the resonant signal. This causes a deformation of the resonance into a so called Fano profile, as indicated in figure 4.2. For simple spectra with maybe a few well separated resonances, one can still easily recognize the separate peaks and guestimate their original location. However, as soon as more complex materials are measured, such as for example organics, many peaks will start to overlap, resulting in an unrecognizable spectrum. This in itself is one of the major drawbacks of CARS microscopy: spectra can be drowned and deformed until they are no longer recognizable.

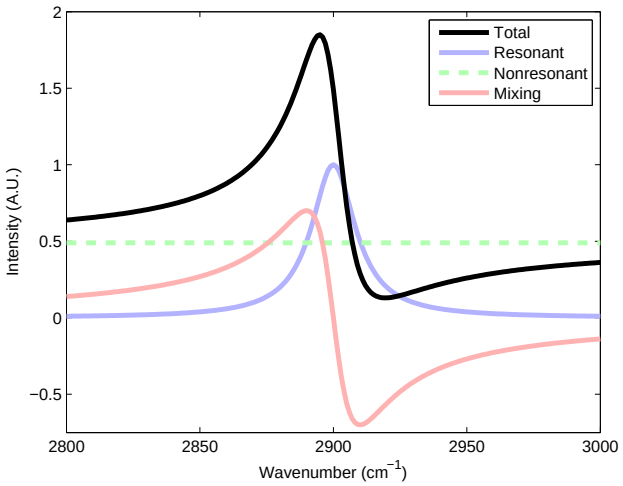

Figure 4.2: Interference from the nonresonant background with the resonance causes a deformed signal in CARS.

4.2 SRS

An alternative to CARS is SRS - Stimulated Raman Scattering. While the underlying physical principles are the same as in CARS, proper detection of SRS signals usually is a bit more difficult.

In SRS, the sample is illuminated by the same two lasers as in CARS: a pump beam with frequency ω_p and a Stokes beam with frequency ω_s. When the difference frequency of those two beams, $\Delta\omega = \omega_p - \omega_s$, matches the energy of a vibrational state, the interaction between the pump and Stokes beams and the vibrational level result in a slight difference in power of the pump beam.

Figure 4.3 shows a schematic energy diagram of the SRS process. With the pump beam exciting the molecule and the signal beam both stimulating emission and exciting again, the field of the SRS induced pump beam is given by

$$E_{P_{SRS}} = \chi^{(3)} E_p E_s^* E_s \tag{4.6}$$

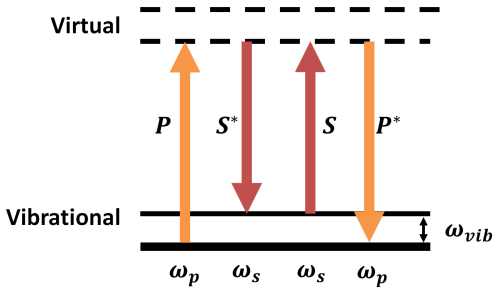

Figure 4.3: Schematic energy diagram showing the principles of SRS.

This light combines with the already existing pump light. The imaginary part of $\chi^{(3)}$ interferes destructively with the pump so that the transmitted pump amplitude after interaction with the sample is given by

$$\begin{aligned} E_{p_{transm}} &= E_p - \mathrm{Im}[\chi^{(3)}]E_p E_s^* E_s \\ &= E_p(1 - \mathrm{Im}[\chi^{(3)}]I_s) \end{aligned} \tag{4.7}$$

Thus, the total transmitted intensity is expressed as

$$\begin{aligned} I_{p_{trans}} &= I_p(1 - \mathrm{Im}[\chi^{(3)}]I_s)^2 \\ &= I_p - 2\ \mathrm{Im}[\chi^{(3)}]I_s I_p \end{aligned} \tag{4.8}$$

In the last step, the term $I_s^2 \mathrm{Im}[\chi^{(3)}]^2$ is dropped because of the small value of $\mathrm{Im}[\chi^{(3)}]$ and the even smaller value of its square.

The first term of equation 4.8 is the original pump intensity, while the second term represents the loss due to SRS. This loss, ΔI_p, is usually around 4 orders of magnitude smaller than I_p [23]. Using a normal photodetector, these differences would be lost in the laser power noise. Since this laser power noise consists mainly of relatively low frequencies, modulating the pump or Stokes beam at high frequencies (in our case, 9.4 MHz) can isolate the desired effect using a lock-in amplifier.

The beauty in SRS is that whenever the difference frequency $\Delta\omega$ does not match a vibrational mode, there is no stimulated emission that interferes with the incoming light and thus no SRS signal: SRS does not have the same non-resonant background that is present in CARS! The trade-off can be found in having to compensate for other background signals such as thermal lensing and two-photon processes which piggyback on the modulated signal. Fortunately, thermal lensing can be corrected for relatively easily. It is an effect that builds up during excitation and thus has a phase shift compared to the desired SRS signal. Using a lock-in amplifier most unwanted signal can thus be removed. For the two-photon absorption there is currently no easy way to distinguish it from the SRS signal. Ultimately, the biggest drawbacks of SRS are longer required imaging times (due to lower sensitivity of the photodiodes when compared to PMT's), the necessity of a lock-in system and these new background signals. Still, this method is many times faster than a regular Raman measurement.

Chapter 5

Setup

For all measurements and imaging a setup was used that has been developed, built and continuously expanded over the past few years. Much of the hardware has been interlinked, so that the setup can be used for CARS, SRS, VPC CARS and more techniques with minimal changes to the settings.

5.1 CARS Setup

The setup can roughly be split into two parts: Signal generation and signal acquisition.

5.1.1 Signal generation

Signal generation starts with an aeroPULSE fiber system (NKT Photonics) laser that outputs 5 ps pulses at 1035 nm with an average power of about 10 W. Part of this beam is immediately frequency doubled to 517.5 nm. The remaining 1035 nm beam is aimed at an acousto-optic modulator (AOM). By using the first order of the AOM while leading the 0th order to a beamdump, the power is reduced to a more usable power. Further tweaking on the AOM enables us to use powers between 0 and ± 200 mW as the 1035 nm fundamental beam. In the CARS process, this beam functions as the Stokes beam.

The 517.5 nm beam is directed into a synchronously pumped optical parametric oscillator (OPO), (APE Berlin, Levante Emerald). The OPO splits the incoming pump beam into two beams following the relation $\omega_{pump} = \omega_{signal} + \omega_{idler}$. By tuning the temperature of the lithium triborate (LBO) crystal and the length of the cavity, the signal beam can achieve wavelengths of 690 nm to 990 nm. The length of the cavity can be tuned with a piezo element while the frequency is finetuned with an intra-cavity rotating Lyot filter. The idler beam is not used in the current setup.

The laser and OPO are controlled and monitored via one computer and the OPO control terminal. A home-written Labview program monitors the power of the signal beam as well as its wavelength, enabling it to display the wavenumber that is currently being probed. A subsection of the program can be used for later hyperspectral imaging, functioning as trigger for the multi-frame imaging on the microscope and adjusting the Lyot filter and thus the probed wavenumber between subsequent frames. Under ideal circumstances this can yield a range of approximately 180 cm^{-1} before the temperature needs to be adjusted.

In the central part of the setup, lenses, dichroic mirrors, delay stages and (flip) mirrors are available to enable alignment of both beams both spatially as well as temporally. Half

waveplates are used to change the polarization of the beams and combined with polarizing filters to attenuate the signal beam. This way, the signal beam power can also be varied between 0 and 250 mW. When the beams are fully overlapped, they are directed into a FV300 scan unit (Olympus). This box contains a set of galvanometric mirrors which are used to deflect the beam in the X and Y direction so that 2D scanning of a sample is possible. Depending on the area that is being scanned and the desired quality of the image, this can take from 0.5 sec (fast scan, no averaging) to minutes (slow scan, multiple averages). Most scans performed during this thesis took about 15-20 seconds per probed wavenumber, using 2-3 averages per image. After deflection, the scanning beam enters the side of the Olympus IX71 microscope, where signal acquisition takes place.

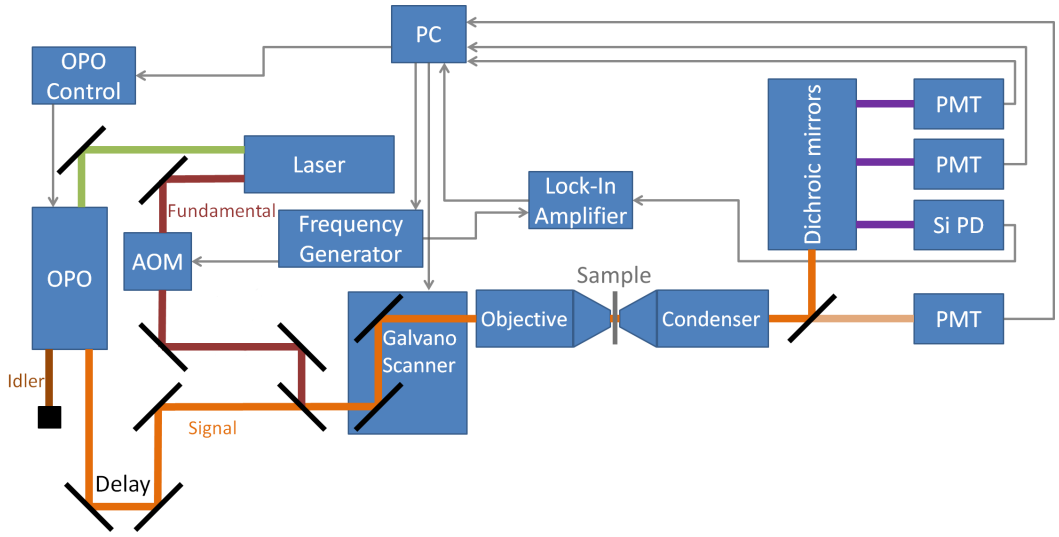

Figure 5.1: Schematic representation of the setup. The box labeled Dichroic Mirrors contains multiple (dichroic) (flip) mirrors and filter wheels to direct the signal to the desired detector(s).

5.1.2 Signal acquisition

Entering the side of the microscope, the scanning beam is reflected upwards, passes through an empty filter wheel (which can be used for epi-CARS) and hits the sample from below. An Olympus UPlanFl 20x/0.5, an UPlanSApo 20x/0.75 and a UPlanSApo 60x/1.20 water dipping objective are available to focus the light onto the sample. Note that the actual scaling/zooming is not only a result of the objective used but also of the scanning angle of the galvanonmetric mirror set. Unless stated otherwise, all measurements discussed in this thesis are taken using the UPlanFl 20x/0.75 objective.

After passing through the sample on an XY stage, all light is collected by either a long-working distance condenser (N.A. 0.55, Olympus XI71 native) or a short working distance water-dipping condenser (LUMPlan FL N 60x/1,00 W). The latter is usually used for fingerprint measurements due to its better transmission characteristics at longer wavelenghts but requires the use of a cover slip, which might influence the morphology of the sample tissue. The collected light is then reflected horizontally to a collection platform. Any light leaking around the mirror is detected via an external PMT connected to the microscope using a fiber cable. The signal collected here can be compared to a regular "transmission image" of the sample.

The collection platform houses 3 detectors: A Hamamatsu R3986 PMT for high wavenumber region measurements, a Hamamatsu R943-02 PMT for fingerprint measurements due to better near-IR characteristics, and a Thorlabs FDS 1010 Si photodiode for SRS measurements. Various flip mounts with (dichroic) mirrors as well as a filter wheel make sure the collected light reaches the correct detector, as well as blocking any possible unwanted signals such as the fundamental beam. For high wavenumber CARS measurements, this usually meant a combination of two 650/60 bandpass filters and two 785SP filters. For most fingerprint CARS measurements, a combination of a HQ 790/95 bandpass filter and a 785/60 bandpass filter was used.

Data from the PMT(s) is collected and processed in the program FluoView, where scan speed, resolution, magnification and PMT sensitivity can also be set.

5.2 SRS Setup

Since SRS uses the same laser beams as CARS, only a few adjustments need to be made to the signal generation. The AOM is no longer used to pass a DC laser signal (of the fundamental beam) but is set to modulate this beam at 9.4 MHz using a GW Instek SFG-2110 frequency generator. Since an SRS signal can be detected as a slight power loss in the pump beam, typically less than 0.01% of the total power [23], lock-in methods are required to separate the SRS signal from the initial beam. This results in a modulated SRS signal which is captured by the Si PD. This photodiode is linked to a HF2Li lock-in amplifier (Zurich Instruments), which uses the reference from the earlier mentioned frequency generator to extract the SRS signal.

For these measurements, the light beam was redirected from the PMTs using a 770SP filter at 45 degrees, after which the beams passed through two 1000SP filters before hitting the photodiode.

Chapter 6

Sample preparation

As mentioned before, this thesis is part of a larger project being carried out by the University Medical Center Groningen and the University of Twente. As a result, most of the samples imaged for this thesis were supplied to us by the departments of Gastroenterology and Hepatology and Medical Oncology at the UMCG.

One of the reasons for using Raman and CARS is the fact that they are label-free methods. They don't require any additives in the sample in order to perform measurements. In fact, many additives will usually provide a false signal, which we wanted to reduce as much as possible. Therefore, tissue was requested that had not been treated in any way, except for extraction and freezing at -80 ^{o}C. The tissue was transported from Groningen to Enschede on dry ice, and placed into a freezer until further processing.

6.1 Initial samples

Some of the first samples to be measured were coupes of a HCT 116 xenograft tumor. These were originally thought to be untreated samples, but it soon turned out they were deparaffinized paraffin coupes treated with either IgG or Cetuximab, as well as containing an IRDye-800CW tracer. As a result, these samples were soon replaced, but they still provided us with valuable information on our processing algorithm.

The next, correct, samples were small patches of xenograft tumor tissue of the cell line A2780. These cells originate from epithelial cells of a human ovarian cancer. These cells had been injected into a mouse and were harvested after they had grown into a small tumor. These tissue samples still needed to be cut into slices and placed on microscope slides, how this was done is explained in section 6.2. Only few measurements have been performed on this tissue as we were informed the tumor had been cut out very accurately, not leaving much healthy tissue around it. Comparing between healthy and tumorous tissue would thus be quite difficult.

In some cases, a quick disposable sample was required to test and align the setup or look for sensitivity in certain wavenumber regions. In these cases, an epithelial cheek cell of the author was taken by swiping a cotton swab along the inside of the cheek. By gently rolling this swab over a microscope slide, some cheek cells would be transferred to the slide and could immediately be imaged.

In situations where the fingerprint region sensitivity of the setup was investigated, a Mannitol sample was typically used. This crystalline powder has a few strong peaks in this region

and was an ideal candidate. Preparation of a test sample consisted of simply depositing a tiny amount of powder on a microscope slide and placing a cover slide on top to prevent the Mannitol from being disturbed by air currents.

6.2 Main samples

The main sample that was used later was a mouse leg that was left over from previous tests at the UMCG. In contained a tumor of the lung cancer cell line Calu-3 which was completely untreated. Because we were not the only one expressing interest in this sample, a piece of roughly 5*5*5 mm was cut out from what was assumed to be the border region between the tumor and the healthy tissue. This was done at the Developmental BioEngineering (DBE) group at the University of Twente, since they have more experience handling biological tissues than OS. The rest of the leg was used by the other party that expressed interest.

Following the extraction, the sample was placed in a small mold, embedded in liquid Cryomatrix and then left to freeze solid in a -20 ^{o}C environment. The Cryomatrix is intended to serve as a fixture during the cryosectioning; cutting the sample into thin slices. Cryomatrix was chosen instead of paraffin - which is a usual choice in combination with formalin for fixating and preserving tissue - because paraffin has a strong Raman footprint [24] and would thus have influenced our results. Cryomatrix on the other hand has a couple of advantages: It has a flat Raman spectrum in the region where we originally wanted to measure ($\pm$ 1500-1700 cm^{-1}) [25] and is supposed to be easily removed by dipping the sample in water. Furthermore, later measurements indicated that in the high wavenumber region - too - there was little interfering signal. What signal remained was easily removed with further processing methods.

Once the sample was frozen solid in the Cryomatrix, a member of DBE (initially Parthiban Periyasami, later Shaun Burer) used the cryotome to cut the sample in thin slices of 7 µm thick. This thickness was chosen to ensure only a single cell layer would be imaged. Multiple slices were positioned on multiple glass slides, as indicated in figure 6.1.

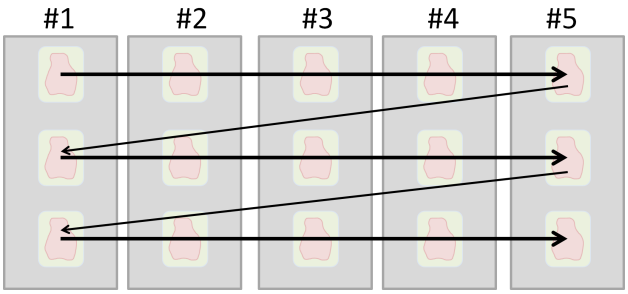

Figure 6.1: Overview of the prepared samples on thin coverglasses. A similar set (# 6-10) was created on a set of regular microscope slides.

Slides #1 to #5 were very thin microscope cover slides, while slides #6 to #10 were regular microscope slides. The thin cover slides were selected because the focal distance of the 60x objective in the microscope is so short that it could only image *inside* the regular glass slide.

Slides #3 and #8 were intended to be reference slides for the DAPI and FISH processing, as will be explained below.

All slides were then stored at -20^oC until they were needed.

6.3 FISH & DAPI staining

Nearing the end of this research, more information was required about what regions of the sample consisted of healthy, and which consisted of cancer tissue. Originally, Hematoxyline-Eosine (H&E) staining was considered, but due to the lack of materials and experience with different methods, members of the neighboring research group Medical Cell BioPhysics (MCBP) suggested DAPI staining and fluorescence in-situ hybridization (FISH).

DAPI is a blue fluorescent stain that binds strongly to DNA and thus can be used to identify the cell nuclei in a tissue. Considering tumor tissue has more DNA and denser cells in general, one can differentiate between tumor and healthy tissue based on the density of the DAPI signal. In FISH, fluorescent probes are attached to *specific* DNA sequences. In this case, the DNA sequences targeted were human sequences. Since the tumor tissue was humane while the healthy tissue originated from a mouse, any difference between tumor and healthy tissue should be very obvious.

Using the DAPI and FISH results to tell the healthy tissue apart from the tumor tissue, a map can be created by performing a mosaic scan over a full sample of for example slide #3 or #8. Depending on how much all samples look alike, this map can then be used to guide the location of new measurements.

The downside of these two methods is that the fluorescent labels will influence the detected CARS spectra. Therefore, these methods were only applied to samples # 3 and 8, so that these results could be compared to the neighboring samples, # 2, 4, 7 and 9. In the case of sample #5, we first performed CARS measurements on random locations within the sample and later checked the tissue distribution using FISH on that same sample.

All DAPI and FISH procedures were carried out by members of the MCBP group.

Chapter 7

Data Processing

The current setup enables us to record both CARS and SRS signals for multiple wavenumbers by imaging the sample multiple times - each time slightly varying the wavelength of the signal (pump) beam resulting in a different vibrational frequency being probed. Due to limitations of the OPO that is used the scan range is usually limited to several nanometers which results in a maximum scan range of 100 to 180 wavenumbers. Through careful adjustment of the OPO crystal temperature during measurements, this range can be extended to up at least 300 wavenumbers in some cases, but these results are difficult to reproduce. Furthermore, some power jumps are usually introduced which can have an adverse effect on the further processing.

Scanning a sample over a range of wavenumbers results in a 3-dimensional data stack. Considering this stack from the XY plane provides a 2-dimensional image of the resonances at a specific vibrational frequency. Taking another approach, viewing the stack along the (vibrational) frequency axis, yields a resonance spectrum for every pixel in the image.

Before any raw datastacks are displayed as an image or processed any further, a few small corrections and adjustments are made. The first is a power correction, where the signal intensity at a specific wavenumber is corrected for the current laser power, so that the full spectrum displayed can be considered to be scanned at constant power. Secondly, a singular value decomposition (SVD) algorithm based on [26] is used to remove some noise from the spectral scans. Finally, the recorded spectra are interpolated so that $\Delta\omega$ is identical along the whole spectrum. This is not the case in the raw data due to the uneven steps made by the OPO, but is required for the Fourier transformations later on. As such, all data labeled 'Original data' will not have undergone any thorough processing, but will have been power corrected and have some noise removed.

7.1 Hyperspectral imaging

In the most simple forms of imaging, the obtained data is usually a 2D-array containing intensity values for X and Y coordinates. The most common way to display this data is to use a grey-scale image where the pixel intensity is directly linked to the measured data value. Typical examples of these kinds of measurements are (digital) black and white photographs or microscope scans at one specific frequency.

Further advanced images contain multiple 2D-arrays which are displayed together. As soon as two or more 2D-arrays are concerned, one could also talk about a datastack. The separate arrays retrieve their data from different sources. This would be the case when not

one, but three vibrational frequencies are probed in succession or simultaneously - as long as the contributions can be linked to the frequency (e.g. three images taken at ω_{vib1}, ω_{vib2} and ω_{vib3}). These datastacks can also be created by combining the results of a single CARS measurement at one vibrational frequency with the intensity results of two-photon-excited fluorescence (TPEF) and second harmonics generation (SHG) measurements as has been done in [27]. In all these cases, the three separate arrays can each be assigned a color (red, green and blue), after which they can be merged into a single RGB image which still has all of its information.

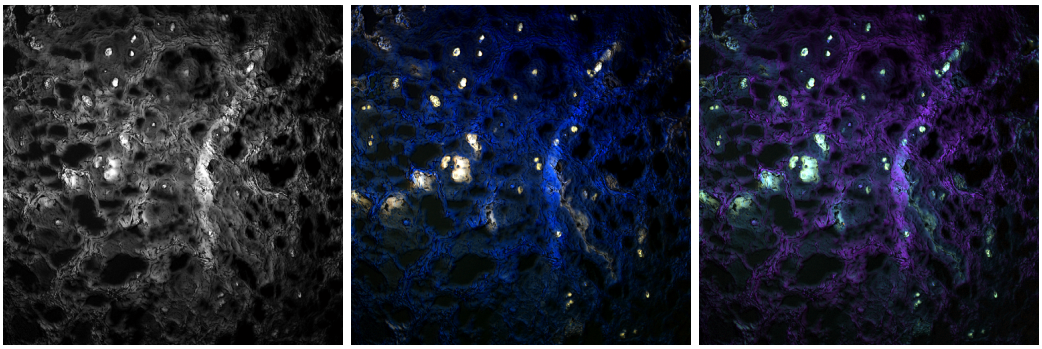

(a) (b) (c)

Figure 7.1: Black and white (a), RGB (b) and hyperspectral (c) images of the same sample. (a) Shows morphology but little chemical contrast. (b) Already isolates the fat parts from the rest, but one can't be sure whether there are any other interesting spectral features outside the three wavenumbers displayed in RGB. (c) Provides a full spectral image and shows some more nuances in the coloring. All displayed data in this example are extracted from a single CARS measurement.

Most measurements performed for this thesis however contain 50-100 scans of the sample forming a *hyperspectral datacube* of x*y*z datapoints where x and y are the number of pixels in both directions and z is the amount of frequencies probed. Every scan contains the measured CARS intensity for a different vibrational frequency, thus providing a spectrum for each pixel. Due to the amount of datapoints per pixel, simple RGB mapping is no longer a viable option. Therefore, a different projection method was used.

Instead of assigning three color channels to three datasets, the full hyperspectral datastack is mapped onto a rainbow color lookup table. This way, every slice representing one vibrational frequency is assigned a specific color hue, while the intensity is still the direct result of the datapoint value. The datastack is then flattened along its frequency axis using additive color mixing and a maximum intensity projection. The final intensity of each pixel will thus be determined by the highest intensity reached over the full spectrum instead of the average. The resulting image is still 'just' an RGB image, but the colors are now a qualitative representation of the spectral features. Broad peaks in the spectrum for example will result in lowly-saturated and bland colors, while strong narrow peaks result in highly-saturated colors. Figure 7.2 gives a quick impression of this method on a mix of paraffin and PMMA beads.

One problem that will inevitably rise at some point is that some areas show similar colors while their spectra are different. This can happen for example in cases where one spectrum has a resonance peak in the yellow part of the look-up table, while another spectrum has both a peak in the green part as well as in the red part. Due to the additive mixing, this

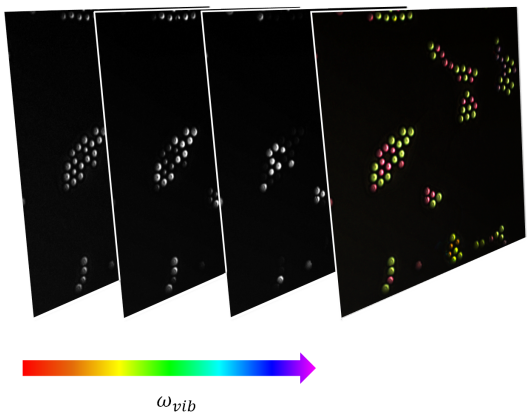

Figure 7.2: Hyperspectral image showing paraffin and PMMA beads. The different resonances result in different colors in the final image.

pixel will turn out yellow as well. In order to still be able to differentiate between those two spectra, the datastack is always processed using three look-up tables instead of just one, creating three different images. The first look up table contains a single rainbow, while the second and third contain two and three respectively. If one would have problems differentiating two colors in one of the resulting images, there is a large chance that the colors are completely different in the other final results. Thus, one can simply choose the colored image that shows most color contrast.

The processing discussed above is done in ImageJ using a macro written by Erik Garbacik during his time as a PhD candidate at the Optical Sciences group.

There are several advantages to the described method. For one, it provides a fast way to visually identify any spectral differences between components in the image. No computing power is required to (iteratively) detect and recognize specific spectra(l resonances) or to perform fits on suspected peaks. Furthermore, no a priori information about the location of peaks or spectral differences is required, any differences show up immediately in the form of color contrast. As a result, this method is very useful for viewing cancer tissue where the difference between healthy and diseased tissue is not (yet exactly) known.

7.2 Extracting a Raman signal

As discussed earlier, spectra retrieved from CARS measurements suffer from mixing with the non-resonant background, while those from SRS measurement are much more like actual Raman spectra. Fortunately, the non-resonant signal in CARS is in phase with the driving force, while the resonance itself has a $\frac{\pi}{2}$ shift. Looking at equation 4.5, we can then see that the resonant term in this equation is complex while any terms containing the non-resonant component are completely real. So, extracting the imaginary part from the total measured signal provides us with a signal that is directly related to the Raman spectrum, free of any non-resonant background. There are several methods to do so. Some, such as VPC CARS [28], involve hardware solutions to simultaneously record amplitude and phase of the signal. While accurate, their application requires experience and additional hardware. Other methods are based on post-processing algorithms, such as the Maximum Entropy Method (MEM) [29] and a method involving a modified Kramers-Kronig (KK) relation [30].

To avoid complicating the setup and because of the limited time span of a Master's thesis, it was decided to use a software-based extraction. Basic versions of both the MEM and a modified KK-algorithm have been scripted in Matlab, after which further research continued with only the KK-version. While the MEM could theoretically be implemented fully automatically, the modified Kramers-Kronig algorithm was chosen because it can deal with larger datastacks much faster than the MEM method. A 512*512*65 datastack for example takes approximately 4 minutes using Kramers-Kronig, while it takes up to half an hour using the MEM. The downside of the Kramers-Kronig method is that it requires manual input of a spectrum that mimics the non-resonant background so that the script has a reference to work with.

A full description of the modified Kramers-Kronig algorithm can be found in [30]. Below, a general but complete summary will be provided. The algorithm used for our data is similar to the one discussed in the paper just mentioned. The main differences are its application to 3D hyperstacks instead of single spectra, as well an integrated singular value decomposition (SVD) denoising algorithm.

7.2.1 Kramers Kronig Explanation

The Kramers-Kronig relation can be used to extract the phase of the signal if the modulus of the susceptibility $|\chi(\omega)|$ is known. Since the measured CARS intensity scales with $|\chi(\omega)|^2$, this is something we know. The Kramers-Kronig relation is given by:

$$\phi(\omega) = -\frac{P}{\pi}\int_{-\infty}^{+\infty}\frac{ln|\chi(\omega'')|}{\omega''-\omega}d\omega'' \tag{7.1}$$

where P is the Cauchy principal value. Unfortunately, this function is only valid if the data covers the entire infinite frequency domain. Several groups, including [30], have developed workarounds for this problem by switching to the time domain and using Fourier series approaches. Most calculations are then performed in the time domain, after which the results are transformed back into the frequency domain for the final calculations. This is done by defining an operator that transforms the spectrum to the time domain, multiplies it with the Heaviside function and transforms it back to the frequency domain. Rewriting this operator and substituting it in equation 7.1 results in the following final equation:

$$\phi(\omega) = 2\mathrm{Im}\left\{\psi(ln|\chi(\omega)|) - \frac{ln|\chi(\omega)|}{2}\right\} \tag{7.2}$$

where the function $\psi(f(\omega))$ deals with the transformations of the original signal to and from the time domain, as explained later on. The desired imaginary part of the complex third-order susceptibility $\chi(\omega)$ is then easily calculated using $Im\{\chi(\omega)\} = |\chi(\omega)|sin[\phi(\omega)]$. Since Raman scattering scales linearly with this quantity, plotting this quantity will give us the typical Raman spectra that are of interest.

The effect of the transformation of the original signal $f(\omega)$ (using $f(\omega) = ln|\chi(\omega)|$) to and from the time domain, governed by the $\psi(f(\omega))$ term, is best illustrated by figures showing the results. A test spectrum has been generated in Matlab by combining a non-resonant background and several (Lorentzian) resonances following equation 4.5. The spectrum has been deliberately made to resemble the spectrum shown in [30] for easy troubleshooting. The resulting total signal as well as the separate non-resonant background can be found in the left part of figure 7.3.

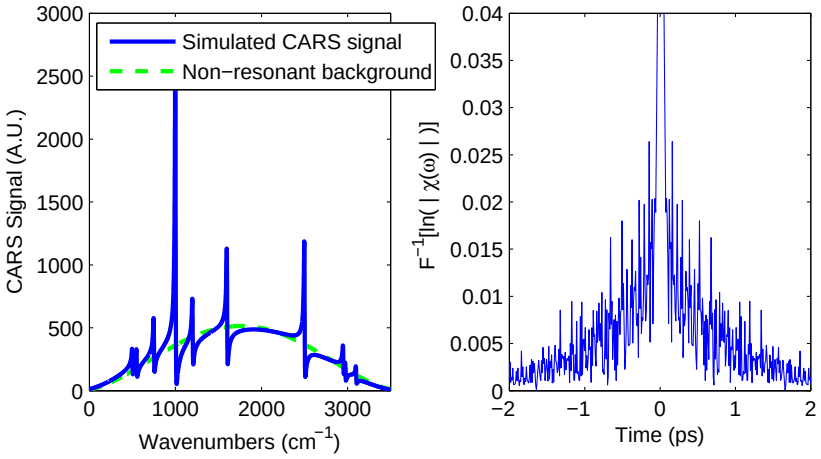

Figure 7.3: Left: Simulated CARS spectrum. Right: Fourier transformed to time domain.

Original transformation of the natural logarithm of the susceptibility to the time domain results in the signal as shown on the right of figure 7.3.

Another requirement to the use of the Kramers-Kronig relation is that the signal should be causal, e.g. it should not exist before t=0. In order to comply with this requirement, all these datapoints are set to be zero. After this, the signal is transformed back to the frequency domain, after which the final calculations (see equation 7.2) are performed. As one can see in figure 7.4, the dip following every resonance (typical for a fano-profile) has been dealt with, but there still is a background signal (variable offset) that is not desired.

This is due to the 'crude' cutting off of all signals at t<0. One can imagine why this is not completely correct: the laser pulse delivering energy to the system is not an infinitely narrow delta pulse, but has a bandwidth as well. Since the exciting pulse oscillates in phase with the non-resonant background, it would be beneficial to place the Fourier transform of the non-resonant component left of t=0. This yields as a final signal

$$\eta(f(\omega)) = \begin{cases} \mathcal{F}^{-1}[f(\omega)] & t \geq 0 \\ \mathcal{F}^{-1}[f_{NR}(\omega)] & t < 0 \end{cases} \tag{7.3}$$

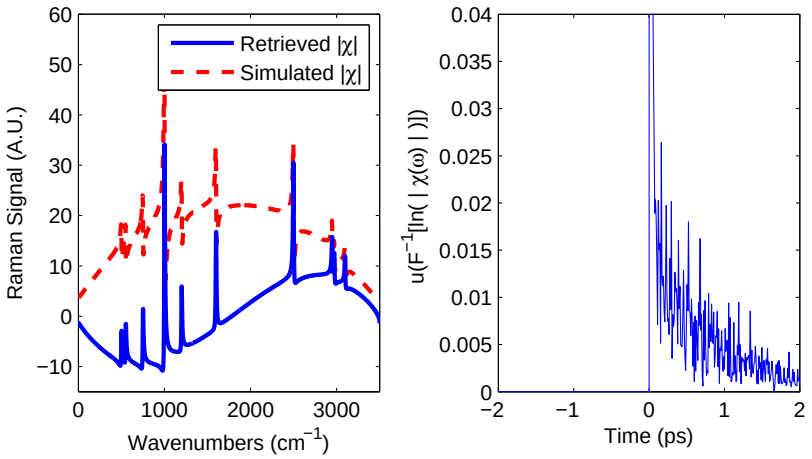

Figure 7.4: Left: Simulated and retrieved Raman spectra. Right: Causalilty by defining values for t<0 to be zero.

As such, the right side of the function still contains resonant and non-resonant contributions, while the left side contains only non-resonant contributions. The resulting figure looks as shown in the right half of figure 7.5. This time, transforming the result back to frequency space and performing the last calculations, the final spectrum looks as shown in the left half of figure 7.5:

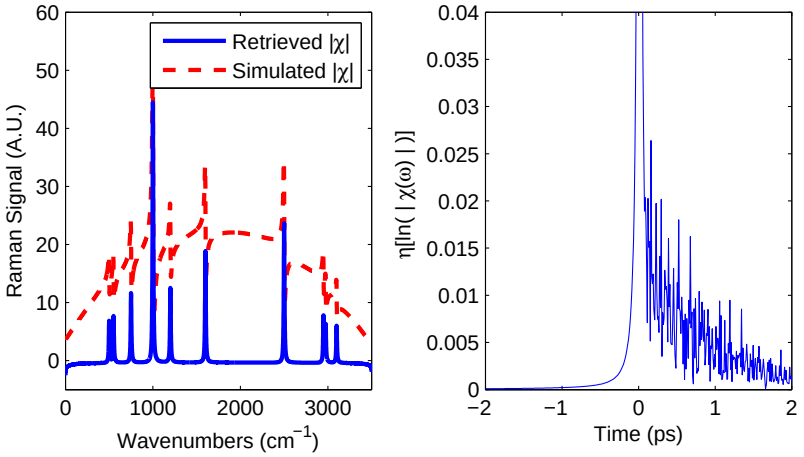

Figure 7.5: Left: Simulated and improved retrieved Raman spectra. Right: Fourier transformed to time domain, combined with NRB transform.

As can be seen, the final result is an accurate representation of the original Raman spectrum. However, one has to consider that in this simulation 3500 datapoints were used (even > 8000 in the original paper), whereas our CARS datastacks usually don't contain more than 50-100 spectral datapoints. To improve the final result, a simple padding procedure was implemented. In an N-sized measurement, N more datapoints were added to the front, and N more datapoints were added to the back of the spectrum, with a value equal to the

first and Nth datapoint respectively. Due to both the padding as well as the limited spectral range of the measurements, the discussed processing method yields best results when no resonances are cut off at the ends of the measured spectral range.

Equation 7.3 needs a reference for the non-resonant background spectrum, so that its inverse Fourier can substitute the t<0 data. We have tried two methods to provide this NRB spectrum. The first method consisted of fitting a first-, second- or third-order polynomial to the measured spectrum and taking this polynomial as the NRB. This way, the broad features of the background would be preserved, while the resonances themselves would not be copied. This worked decently for the simulated spectra, but results were very inaccurate for real sets of data. The resonances were much broader and overlapped much more than anticipated, so that the resulting non-resonant fit still contained resonance components as well. Also, this method required performing a polynomial fit for every pixel, significantly slowing down the processing algorithm. The second method, the one that was later chosen, consists of manually selecting a 3x3 pixel area whose average spectrum is considered to be 100% non-resonant background. The location of this area should of course be some place where there are no resonances in your sample. Good locations for this are usually just outside the tissue or vacuoles inside. As an extra bonus, simulations showed that when this pixel accidentally *does* contain a resonance, it only affects the processing for that specific resonances. While this resonance will be removed from the entire image (together with the non-resonant background), all other resonances will be left unaffected.

Chapter 8

Results

In the following sections, results will be shown of the different steps taken towards hyperspectral imaging of cancer tissue. Data will typically be presented as a set of one (hyperspectral) image with regions of interest (ROI's) marked and a graph showing spectra corresponding to the average spectrum within these respective ROI's. The powers mentioned for the signal beam in hyperspectral measurements refer to the power of the beam at the lowest wavenumber. During scanning, the power would typically increase by 30-50% and then drop to a value slightly lower than the starting power. All data has been corrected for these variations.

8.1 First results with Kramers-Kronig

The results below show some of the first complete measurements performed on tissues. Due to some miscommunication, these were samples of treated tumors, so spectra will also show (traces) of medicine and fixating media. The results are however still very useful to indicate the difference a proper KK-transformation can make.

Figures 8.1a and 8.1c show a typical hyperspectral CARS measurement. The hyperspectral range was about 50 wavenumbers, but as one can see the spectra are very flat and no specific peaks can be recognized. In the unprocessed image, one can see all of the tissue, as well as an example of isolated NRB signal in the lower left corner. Selecting this area as reference for the Kramers-Kronig transformation, the results look as in figures 8.1b and 8.1d. Although the accuracy of the new spectra is doubtful to say the least, the effect of the Kramers-Kronig algorithm on the hyperspectral image is very clear. There is more contrast between the cell types than before. While there is definitely room for improvement, a first step has been made.

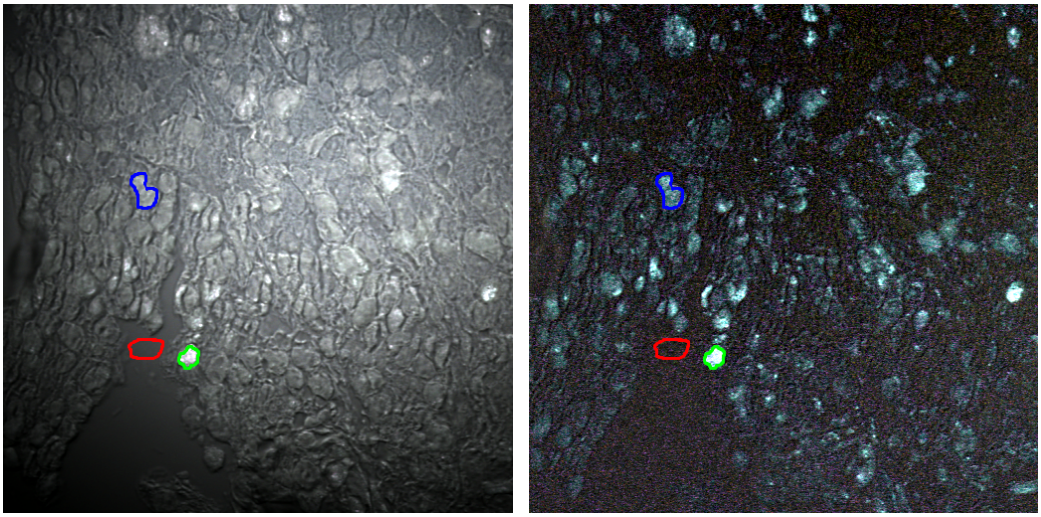

(a) Original CARS image

(b) Processed CARS image

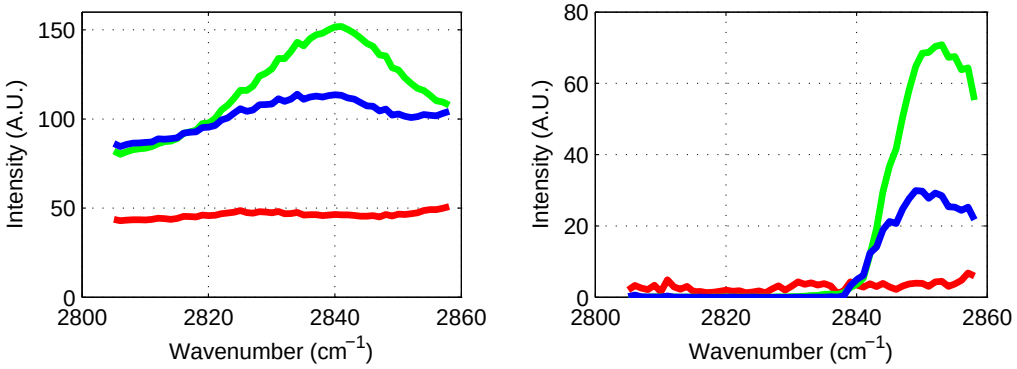

(c) Original spectra

(d) Processed spectra

Figure 8.1: Tumor sample of the HCT 116 cell line treated with IgG antibodies. Deparaffinised paraffin coupe, treated with Hoechst staining and IRDye 800CW tracer. Image taken using a 50 mW signal beam and 200 mW fundamental beam, 2 Kalman averages and 4 µs pixel dwell time. Image edge corresponds to 157 µm.

Figure 8.2 shows similar results, albeit of a different sample and at much higher magnification. Here too, the image starts out as a nearly monochromatic blue image with just a few pink spots. After the processing, different parts stand out much more from the background, and the different colors that become visible indicate other components which were not visible in the original image. While the left half of the spectra appears rather weak, a nice peak around 2850 cm^{-1} can be recognized and explained by lipids within the tissue.

One can notice that the processed images have much higher noise levels than the unprocessed images. To compensate for this, the original images were smoothed using the SVD algorithm. Figure 8.3 shows the difference it makes both in the final image as well as in the spectra.

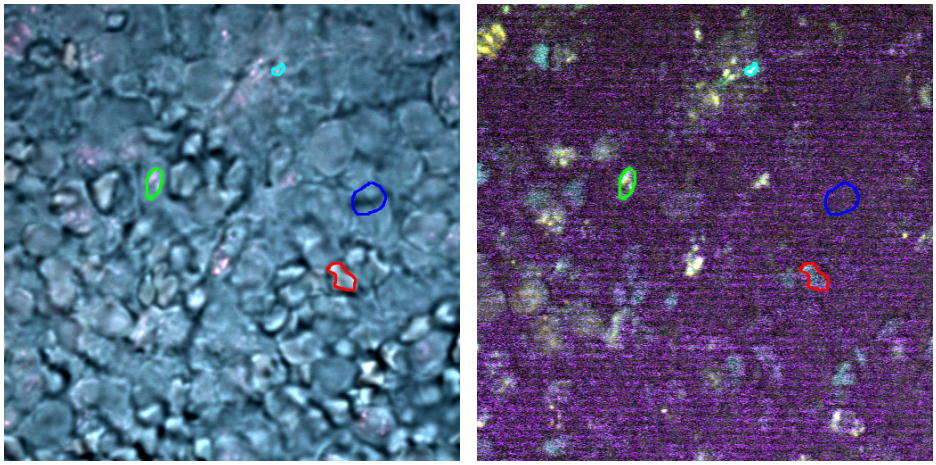

(a) Original CARS image (b) Processed CARS image

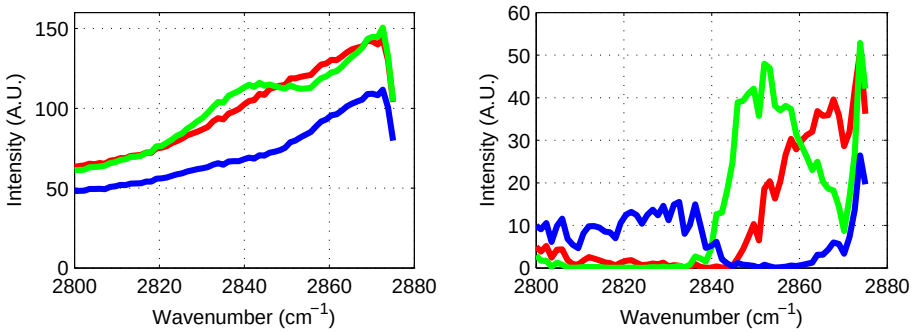

(c) Original spectra (d) Processed spectra

Figure 8.2: Tumor sample of the HCT 116 cell line treated with Cetuximab antibodies. Deparaffinised paraffin coupe, treated with Hoechst staining and IRDye 800CW tracer. Image taken using a 50 mW signal beam and 200 mW fundamental beam, 4 µs pixel dwell time. Image edge corresponds to 59 µm.

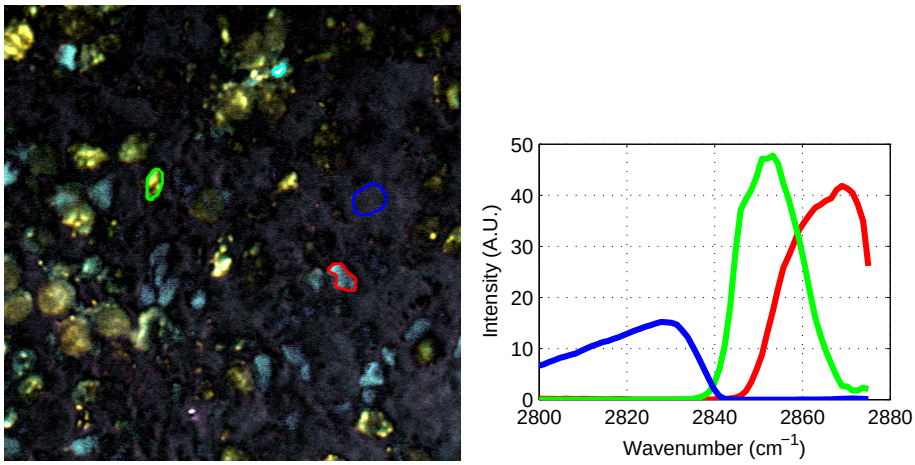

(a) Processed CARS data including SVD (b) Processed spectra including SVD

Figure 8.3: Same data as in figure 8.2, but this time SVD denoising has been applied before the other processing steps.

8.2 Fingerprint attempts

The original idea of this assignment was to look mainly at the fingerprint region since it contains so many specific peaks. While we were aware of the fact that the signal detection would also be more difficult here, the lack of quality of the results as shown below was not expected.

Figure 8.4 shows a typical result of a CARS measurement in the fingerprint region. In this case, a scan was performed from 1390 to 1540 cm^{-1}, covering a broad peak around 1450 cm^{-1} which is typical for both lipids and proteins. The unprocessed image already shows virtually no color contrast and the spectra of the three selected regions look very similar. Processing the data resulted in the image shown in figure 8.4b. Two things that are immediately noticable are the decrease in contrast and the increase in noise levels. Structures within the tissue are more difficult to recognize than before processing. The spectra present in the processed version don't have any similarities with the unprocessed spectra. In fact, all three look just like noise and more interestingly are also very similar to each other. In a simulated spectrum, the ratio between the CARS signal and the non-resonant background was of absolutely no influence on the processed result. Here, however we can clearly see that after processing there is no usefull data left.

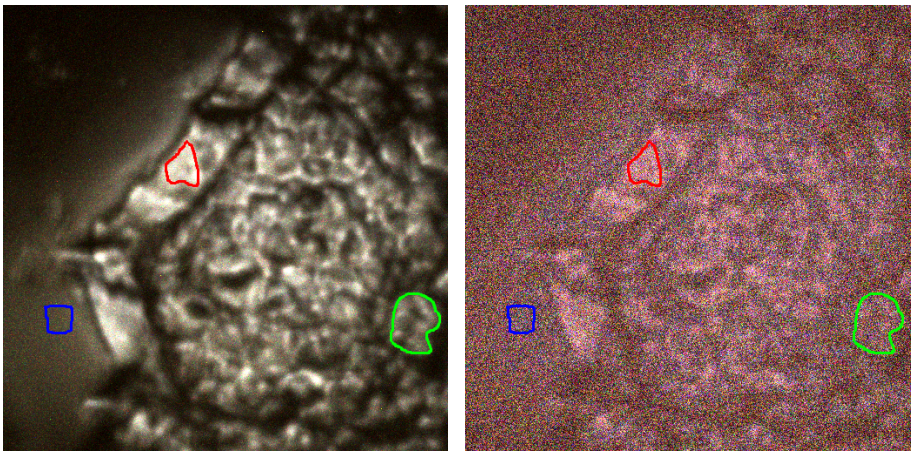

(a) Original CARS image

(b) Processed CARS image

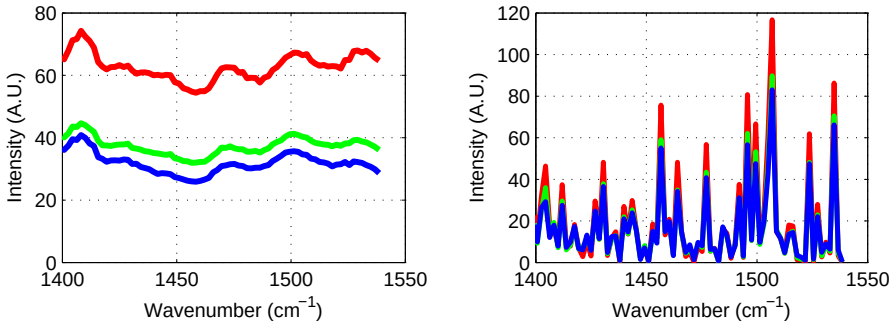

(c) Original spectra

(d) Processed spectra

Figure 8.4: Tumor from cell line A2780 in the fingerprint region. Untreated sample cut in cryotome with Cryomatrix. Image taken using a 75 mW signal beam and 200 mW fundamental beam, 3 Kalman averages and 12 µs pixel dwell time. Image edge corresponds to 200 µm.

Another scan was performed on a cheek cell. The resulting image is shown in figure 8.5a. Here one can again see the extreme similarities between the different spectra. After processing, the result looks as shown in figure 8.5b. In this case, the cell itself has completely disappeared from the image while the surroundings are shown in a single color. A glance at the shown spectra shows that they appear to be the same spectrum with different scaling factors.

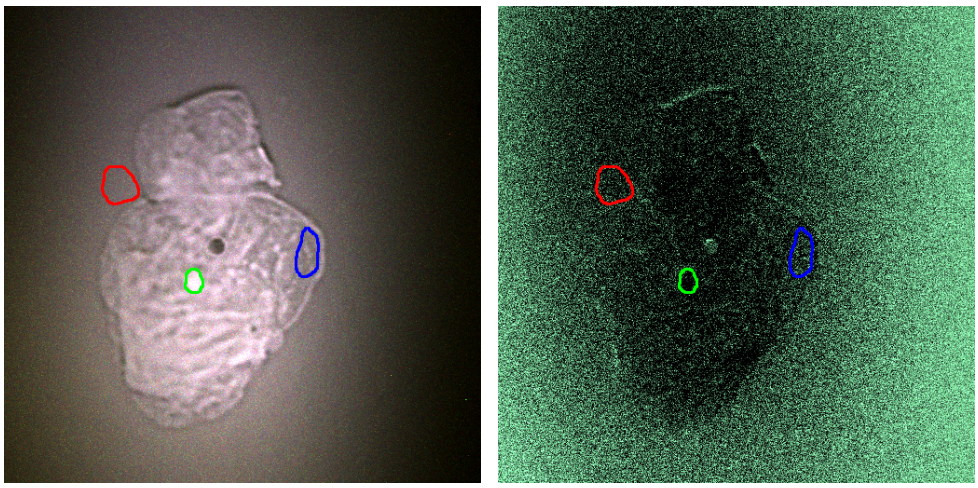

(a) Original CARS image

(b) Processed CARS image

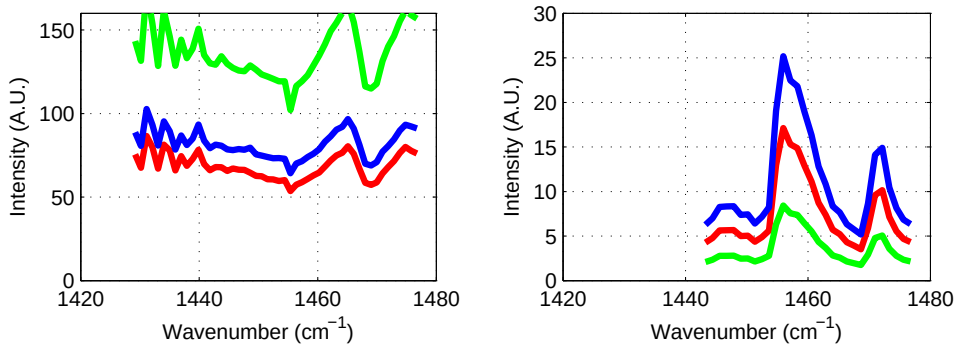

(c) Original spectra

(d) Processed spectra

Figure 8.5: Cheek cell of the author imaged in the fingerprint region. Image taken using a 110 mW signal beam and 200 mW fundamental beam, 6 Kalman averages and 12 µs pixel dwell time. Image edge corresponds to 157 µm.

The two examples above are typical for many fingerprint measurements performed. This led us to believe that the weakness of the resonances in combination with the strong non-resonant background made the datasets unusable for the Kramers-Kronig processing. As such, an attempt was made to image some cells using SRS to compare with, since these would not suffer from the non-resonant background.

Figure 8.6a shows an SRS scan of an epithelial cheek cell at 2920 cm^{-1}. Clearly, in the high wavenumber region, this provides a decent signal. One should note that any pixels that have zero intensity have been color-coded blue. However, moving to the fingerprint region and taking a scan at 1660 cm^{-1} results in the image shown in figure 8.6b. While one can still make out the general shape of the cell, all detail is lost and there is no real usable data.

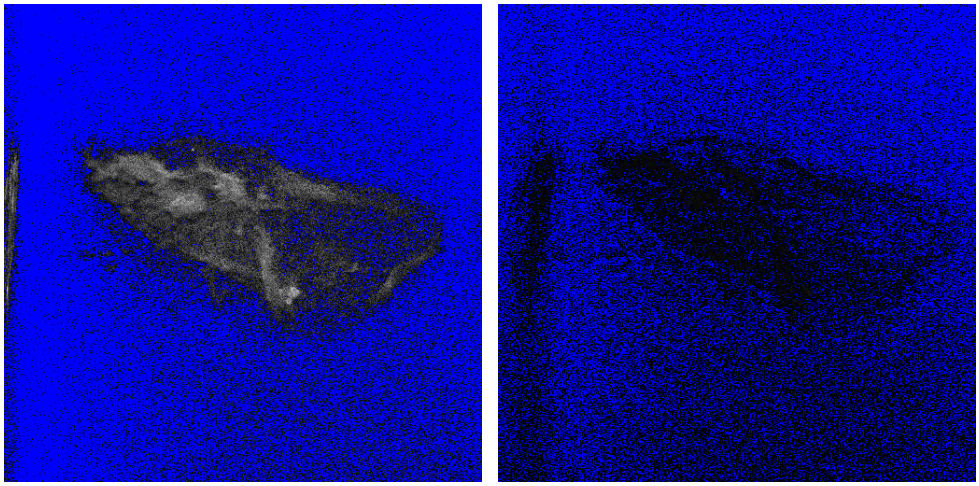

(a) SRS at 2920 cm^{-1} (b) SRS at 1660 cm^{-1}

Figure 8.6: Cheek cell of the author. Image taken using a 60 mW signal beam and 200 mW fundamental beam.

Some measurements were also performed on Mannitol crystals. Those had previously been used and should provide a clear signal - also in the fingerprint region. Figure 8.7a shows the first result of a high wavenumber scan at 2875 cm^{-1} using CARS. There is no signal from the surroundings and the particle can easily be recognized. Switching to the fingerprint region at 1450 cm^{-1} resulted in figure 8.7b, showing a strong fingerprint signal. While the surroundings are no longer pitch black - indicating a slightly lower quality alignment of the beams - we clearly see a signal originating from the fingerprint region. Measurements using SRS were also performed and showed that here, too, decent fingerprint results could be achieved.

The difference between the tissue measurements and the Mannitol measurements can of course be found in the concentrations of the molecules probed: organic tissue contains a lot of water and many types of molecules, whereas the Mannitol is high-grade and contains mostly the same molecules. As a result, it has a much stronger CARS or SRS signal and less non-resonant background. Ultimately we had to accept that with the current setup, the concentrations in organic tissue are too low to provide a decent signal that can be processed. As a result, the focus was shifted towards the higher wavenumber region.

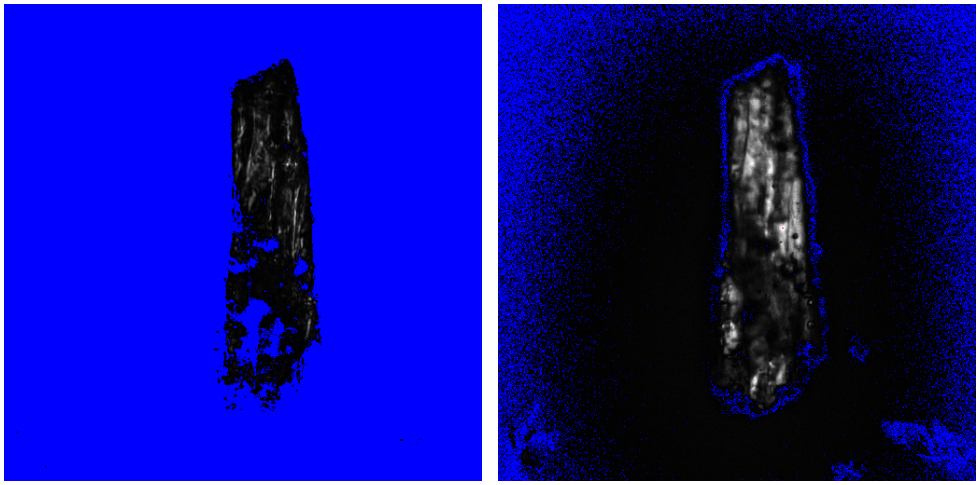

(a) CARS at 2875 cm^{-1} (b) CARS at 1450 cm^{-1}

Figure 8.7: Mannitol crystals in the high wavenumber region and fingerprint region. Images taken using a 100 mW signal beam and 200 mW fundamental beam, 5 Kalman averages and 12 µs pixel dwell time.

8.3 Cryomatrix effects

One set of measurements was performed to analyze the influence of the remaining Cryomatrix on our samples. It should be possible to wash it away with water while keeping the sample intact, but trying to do so sometimes resulted in parts of the sample detaching from the microscope slide. Because of this, we briefly investigated the spectral effect of leaving the Cryomatrix on the sample.

Figure 8.8a shows the raw data. Some tissue is clearly visible, the Cryomatrix is the grey area in the top half of the image. To the left of the image we can see the edge of the Cryomatrix. Figure 8.8c shows the processed hyperspectral image when the area within the cyan circle is selected as a non-resonant background reference. Most Cryomatrix is removed from the image, both in the top half of the image as well as in the holes in the tissue. However, there is a part that still shows a very faint purple color. In the spectrum, this is visible as a broad peak around 2930 cm^{-1} of the blue line. Selecting this region to be the non-resonant background reference instead results in figure 8.8e. Here, that discussed peak has disappeared as well.

One should notice this has had the previously predicted effect on the other spectra: when a resonance is present in the selected non-resonant background pixels, this resonance will be removed from the total signal just like the non-resonant background. Comparing the spectra in figure 8.8d and 8.8f shows that indeed that the signal intensity around 2930 cm^{-1} has decreased while leaving the other resonances virtually untouched. Thus, any resonant peaks belonging to the Cryomatrix will not show up in our final spectra as long as the Cryomatrix is selected as the reference for the non-resonant background removal.

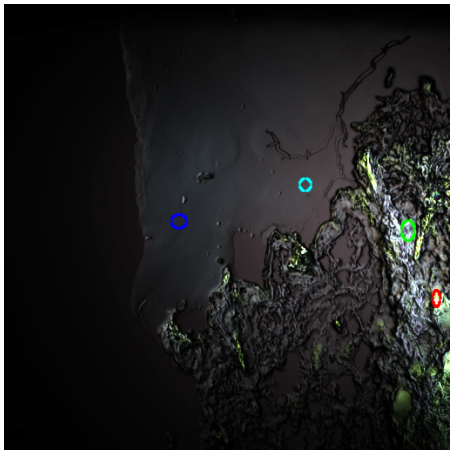

(a) Original CARS image

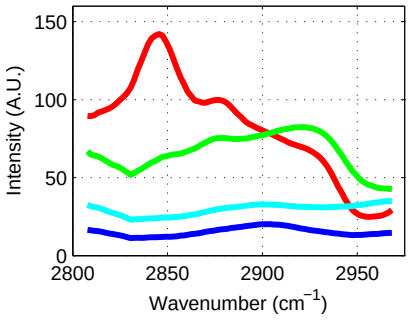

(b) Original spectra

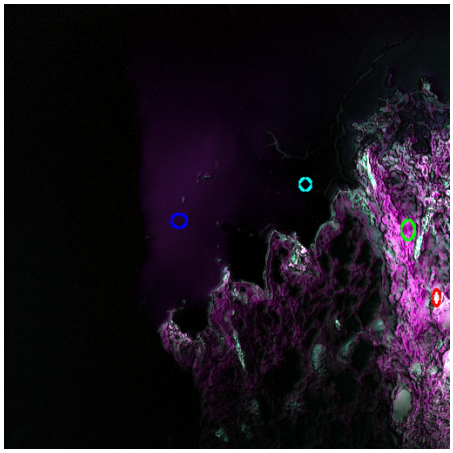

(c) Processed CARS image

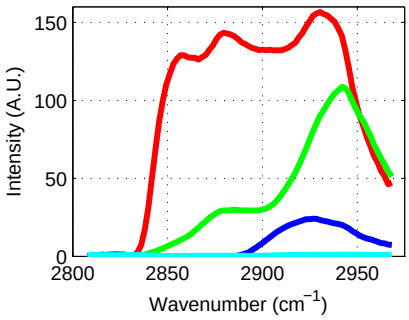

(d) Processed spectra

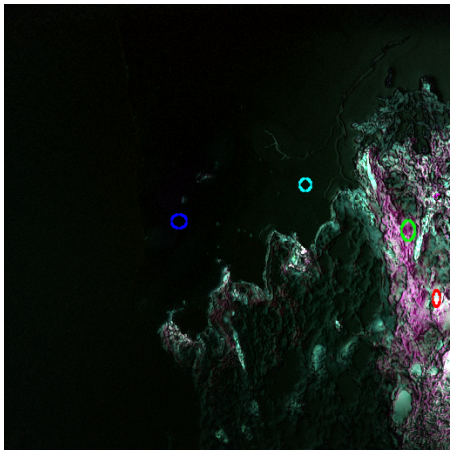

(e) Alternative processed CARS image

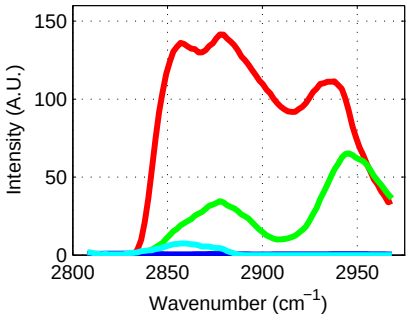

(f) Alternative processed spectra

Figure 8.8: Edge of a Calu-3 tissue sample showing the tissue-Cryomatrix interface and the edge of the Cryomatrix. Images taken using a 100 mW signal beam and 100 mW fundamental beam, 3 Kalman averages and 12 µs pixel dwell time. Image edge corresponds to 700 µm.

8.4 SRS comparisons

To check the accuracy of the Kramers-Kronig retrievals, images created using both CARS and SRS data are analyzed side by side to show differences and similarities.

Figure 8.9 shows the results of a CARS measurement over ± 170 wavenumbers in the high wavenumber region. In the original CARS data (figure 8.9a) one can already see a slight color difference causing two parallel, mostly vertical bands. Looking at the spectra of the marked regions (figure 8.9c) we can see a peak around 2930 cm^{-1} and what might be a faint shoulder around 2890 cm^{-1}. After having applied the Kramers-Kronig processing, we can make a better distinction between the two resonances. Both vertical bands have (relatively) strong resonances at 2930 cm^{-1}, while the tissue to the right also contains a significant resonance at 2880 cm^{-1}. The band with the green ROI also shows a shoulder at 2880 cm^{-1}, but this remains weaker than the main resonance at 2930 cm^{-1}.

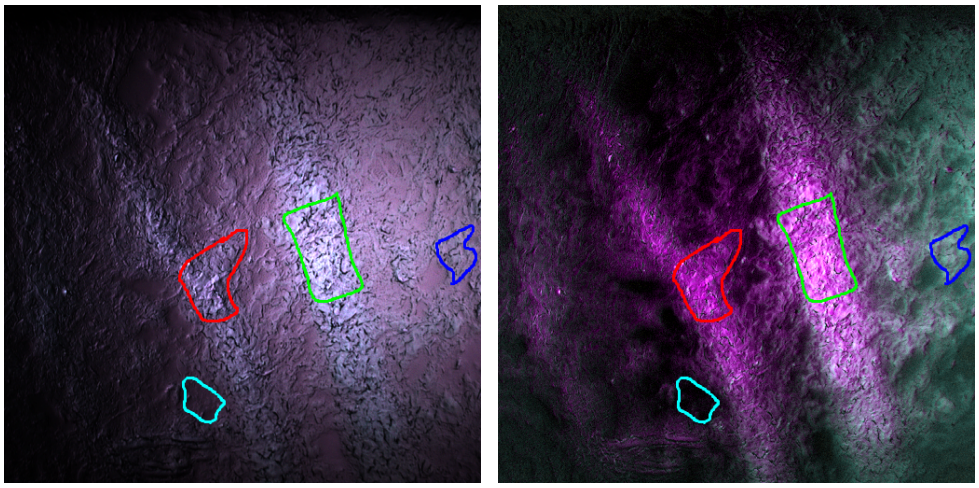

(a) Original CARS data.

(b) Processed CARS data

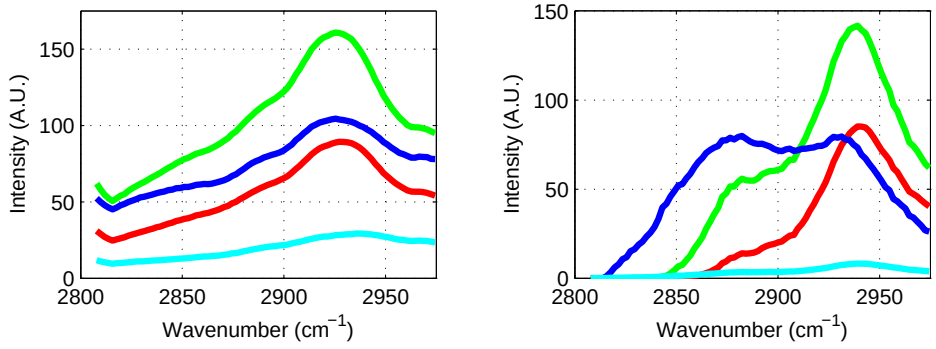

(c) Original spectra

(d) Processed spectra

Figure 8.9: CARS results of the tumor sample of the Calu-3 cell line, untreated. Images taken using a 85 mW signal beam and 100mW fundamental beam, 3 Kalman averages and 12 µs pixel dwell time. Image edge corresponds to 700 µm.

A few days later, the same area was imaged using SRS instead of CARS. The same regions have been marked and the results are shown in figure 8.10. Although the color contrast is less extreme than that in the processed CARS image, the two vertical bands again dominate with strong peaks at 2930 cm^{-1}. The area to the right of both bands again shows a double peak at 2875 cm^{-1} and 2930 cm^{-1}. While there should be no non-resonant background present in this data, we can still see other background sources (note: the Y-axis starts at 20!). These are probably partially two-photon processes as well as some left-over thermal lensing effects. Still, these areas are clearly different from the resonant areas. The small irregularities in the spectrum, such as at 2850 cm^{-1}, are most likely caused by variations in the signal power which have not been perfectly corrected. The steep decline of the signal around 2810 cm^{-1} is thought to be the right side of a lower-lying resonance.

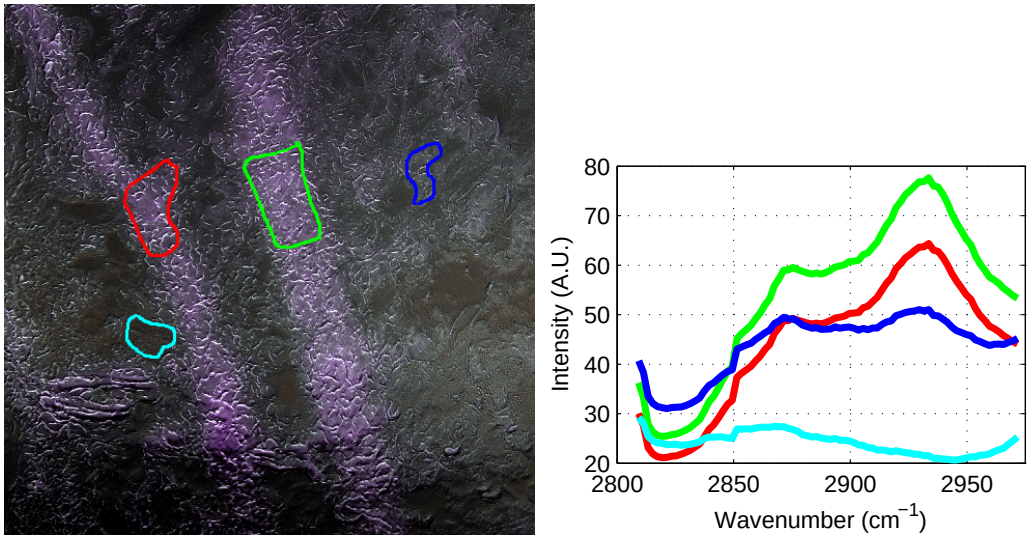

(a) Original SRS data

(b) SRS spectra

Figure 8.10: SRS results of the tissue sample of the Calu-3 cell line, untreated. Images taken using a 110 mW signal beam and 150 mW fundamental beam, 4 Kalman averages and 12 µs pixel dwell time. Image edge corresponds to 700 µm.

Comparing the spectra from figures 8.9 and 8.10, we see that the Kramers-Kronig algorithm has done a good job in extracting the resonant peak at 2880 cm^{-1} which was not visible in the original data. Similarly, the peaks around 2930 cm^{-1} became more clear. The main difference can be found in the red spectrum. For the CARS data, it contains only a minor resonance at 2880 cm^{-1}, while this resonance is significantly stronger in the SRS data. This might be a result of the poorer illumination in that area of the sample but no conclusive explanation could be found.

A second sample was imaged using both CARS and SRS for comparison, but this time the measurements were performed in sequence so that both results perfectly overlap and no changes might have occured in the sample due to storage. Figures 8.11a and 8.11c once again show the unaltered and processed CARS results, with the respective spectra on their right. Several regions have been selected for spectral analysis, based on the color differences in figure 8.11c. One can see a generally pink-like tissue, with yellow regions appearing to lie on top. Other marked areas include the non-resonant background, a fat part (bottom left) and an area containing a mix of the pink and yellow tissue (blue region of interest).

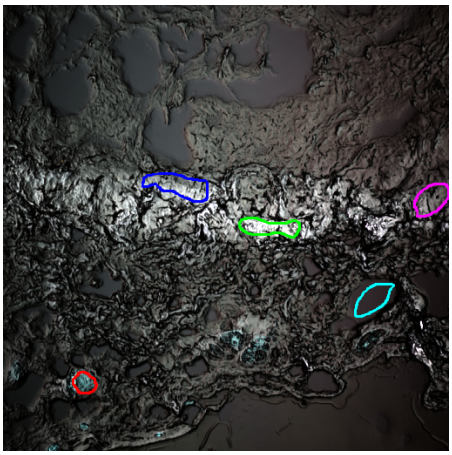

(a) Original CARS image

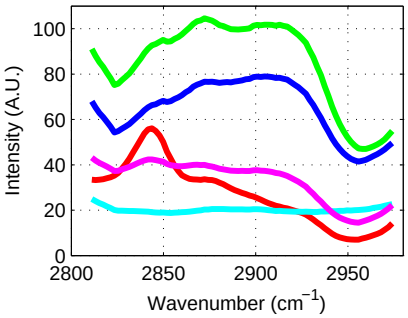

(b) Original CARS spectrum

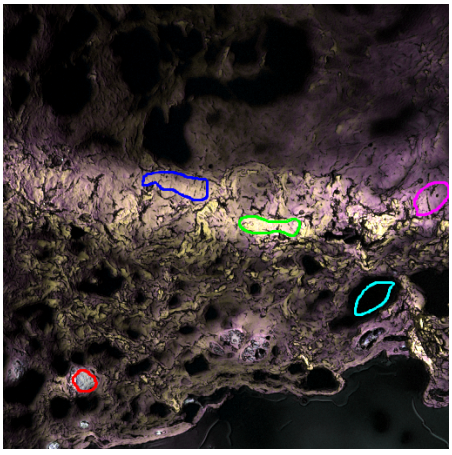

(c) Processed CARS image

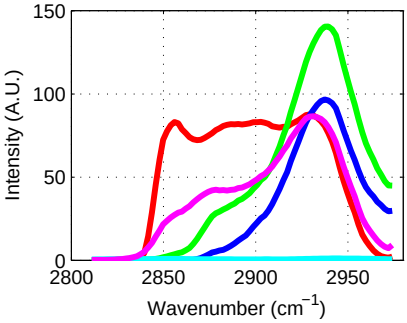

(d) Processed spectrum

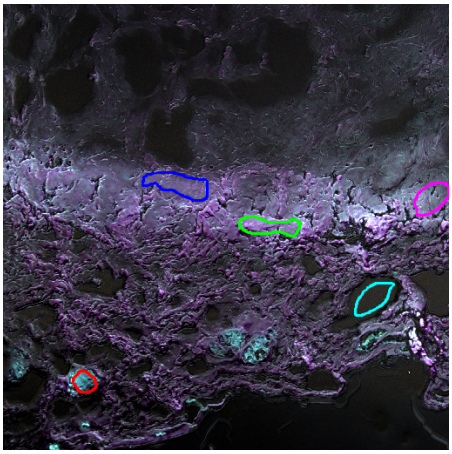

(e) SRS image

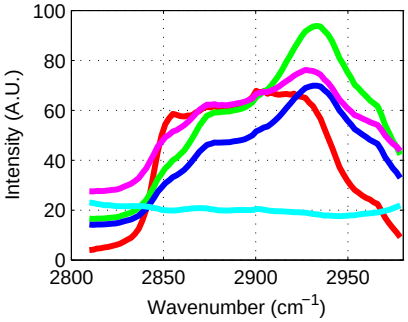

(f) SRS spectrum

Figure 8.11: Comparison between CARS and SRS results of the untreated tissue containing Calu-3 cell line. Images taken using a 105 mW signal beam and 150 mW fundamental beam, 3 Kalman averages and a 12 µs pixel dwell time. Image edge corresponds to 700 µm.

The most obvious features are again a strong peak at 2930 cm^{-1} which has shifted slightly to lower wavenumbers in some cases, a peak just above 2850 cm^{-1} and a shoulder-like resonance around 2880 cm^{-1}.

The SRS image (figure 8.11e) shows less color contrast than the processed CARS results. This is due to the stronger signals in the 2800-2900 cm^{-1} region. In fact, a different color scheme was chosen in order to show as much contrast as possible. Looking at the spectra, we can see the similarities with the processed CARS spectrum, but also many differences. The red spectrum corresponding to the fat blob in the lower left corner fits best, although the peak at 2855 cm^{-1} is slightly less pronounced. More interesting however are the green, blue and magenta spectra. In the SRS measurements the amount of signal for the 2850 cm^{-1} and 2880 cm^{-1} resonances is much higher than in the processed CARS results. The fact that the CARS results appear to have a lower fat content (peaks at 2850 cm^{-1} and 2880 cm^{-1}) than the SRS results was also visible in figures 8.9 and 8.10. It is difficult to find an explanation for this: There doesn't seem to be a cut-off resonance that might influence the CARS results and the SRS measurement appears to be of decent quality too. One possible explanation however might be the presence of a stronger lipid signal in the Cryomatrix than expected. This would explain the signal around 2830 and 2880 cm^{-1} in the SRS measurements and the lacking signal in the CARS measurements, since it would have been removed together with the NRB. Interestingly enough, the fat blob has a very similar spectrum in both images and does not seem to suffer from this problem.

The extra anomalies visible in the SRS spectra (bump at 2980 cm^{-1} and bending at 2900 cm^{-1}) can be explained by a weaker protein vibration and another power issue respectively.

Altogether, the comparisons show that resonances that were previously nearly invisible were successfully isolated from the non-resonant background. The final intensity of the peaks - and thus the quantitative quality of the spectra - can vary, in this case especially in the lipid region. While this should be considered, it should not pose too much of a problem in this research since it will happen in all measurements and thus should not cause spectral difference where there isn't any.

8.5 Final tissue samples

The figures below contain measurements that have been performed during the end of this project, where both the setup and the processing algorithms had been reasonably optimized. It should not be difficult to spot the difference in quality when compared with earlier measurements. First, however, the results and usefulness of the DAPI and FISH results will be discussed.

8.5.1 FISH and DAPI results

Figure 8.12 shows the result of an initial DAPI scan. Due to the size of the sample multiple scans had to be stitched together. The overall shape of the sample is very easy to recognize, with the DAPI having concentrated in cell nuclei. Some areas are seen to have a higher density of dots, mainly in the lower left. Here, the distinct dots have been replaced by slightly smudged out signals. This area was thought to be cancer tissue, but it turned out to be very difficult to use this information. Despite the systematic slicing of the sample slices from the main bulk sample, subsequent slices did not look similar enough to use this image as a guide for measurements on the next sample.

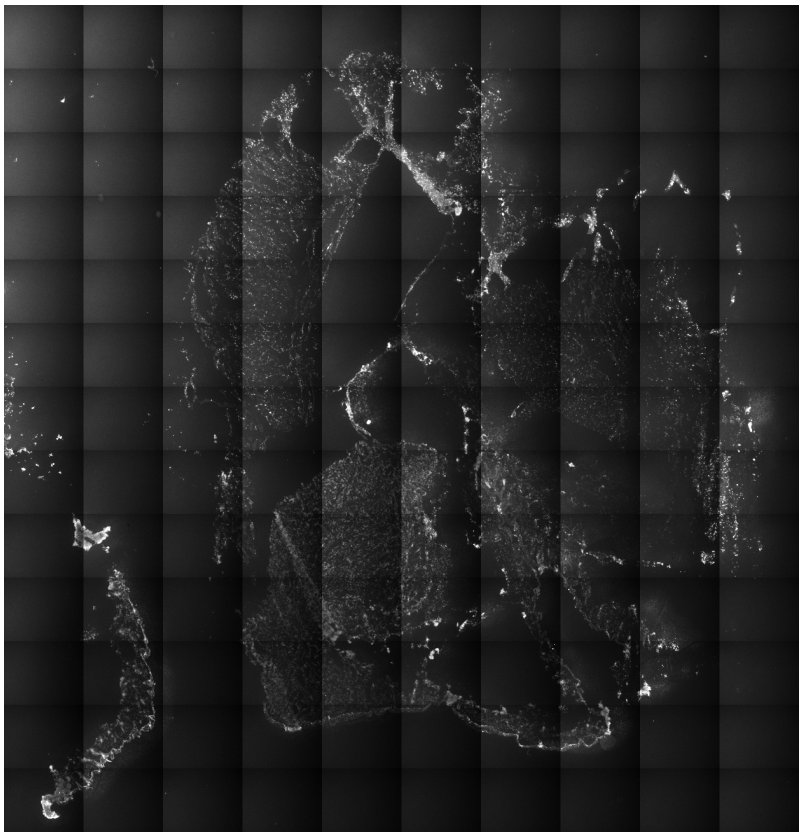

Figure 8.12: Mosaic composite image of multiple DAPI scans. The two diagonal-vertical bands on the bottom right of the main object are thought to be cancer tissue. Contrast has been slightly increased for better visualization.

When it turned out the DAPI measurement was not as useful as initially thought, 6 new scans were performed on seemingly interesting locations on a new sample. Afterwards, this sample was treated with both DAPI and the FISH procedure. The results of this scan are

shown in figure 8.13a. Here, DAPI is displayed in red while the FISH signals are visible in green. At first glance the entire sample appears to be humane tumor tissue due to the abundance of green signal. Most of this however is just background signal. Only the lower left area can be identified as tumor tissue. Looking at a crop of this area in figure 8.13b, a clear difference can be seen between the background signal and the real FISH signal. The real signal manifests itself as small high-intensity spots, marking the DNA locations that are tagged. The background signal, mostly visible on the left, shows more cell-like shapes and is not as concentrated.

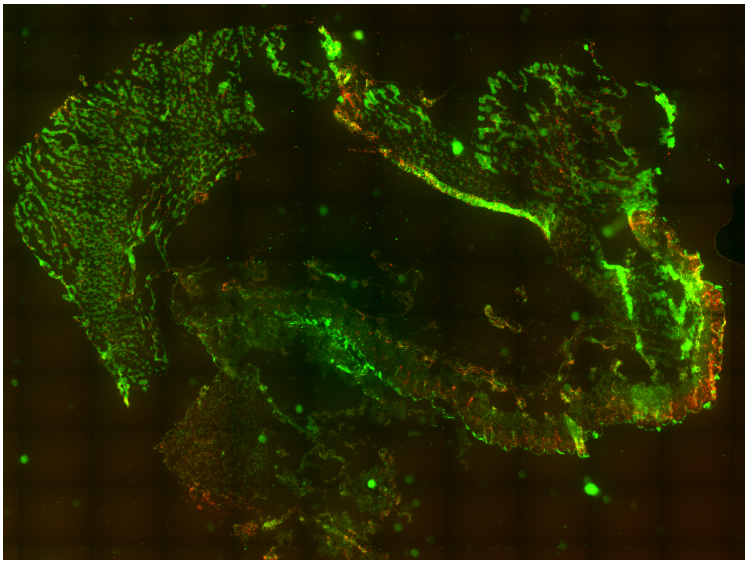

(a)

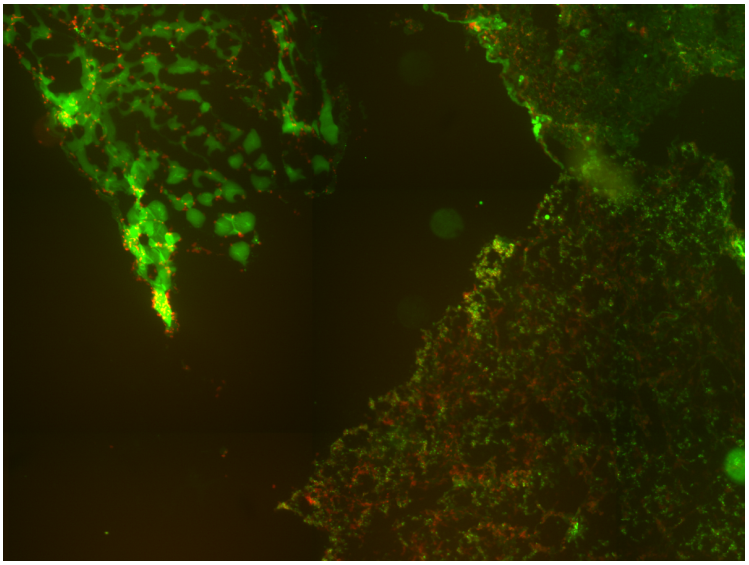

(b)

Figure 8.13: Mosaic composite images of multiple DAPI (red) and FISH (green) scans of sample #5 of the Calu-3 cell line. Figure 8.13b is a crop of the bottom left part of the full image.

The red DAPI signal shows an inverse reaction: in the healthy mouse tissue it shows up as distinct dots, while it looks much more unorganized and spread out in the tumor tissue.

While there are some small patches through the sample that also show the typical cancer-signal for the FISH measurements, they are too small to be of use for our measurements. Other high intensity areas are mostly found around the edges, but this can't be reliably be linked to cancer since these areas could just as well be folded tissue.

Before the FISH and DAPI treatment some areas of this sample had been imaged using CARS. In hindsight, none of these areas covered the identified tumor tissue. As such, attempts have been made to perform new CARS measurements on different sample slices now that the tumor location was known. However, the shapes of the tissue samples were too different from the imaged sample, again making it impossible to image areas that were *known* to be tumor tissue. Thus, all results in the following section show mostly typical measurements, but no clear difference between cancer and healthy tissue can be shown.

Full page scans can be found in the appendix for a closer look.

8.5.2 Tissue scans

In figure 8.14 the results of a scan are shown which was thought to show a clear boundary between healthy tissue on the right and tumor tissue on the left. This idea was based on the low amounts of lipids (2850 cm^{-1} and 2880 cm^{-1} resonances) and high amount of proteins (2930 cm^{-1}) on the left, while the right part contained relatively more lipids. However, it soon turned out that moving or rotating the sample yielded a similar color gradient. Also, by adjusting the location of the NRB-reference the 'border' area could be moved left or right. The error seen in this image thus is an error in the spectrum, based on spatial data (location). This could be caused by a combination of poor alignment and chromatic aberration in the optics although the wavelength difference would have been very small. Still, this remains the only viable conclusion, since re-alignment of the microscope resulted in a better image without color gradient.

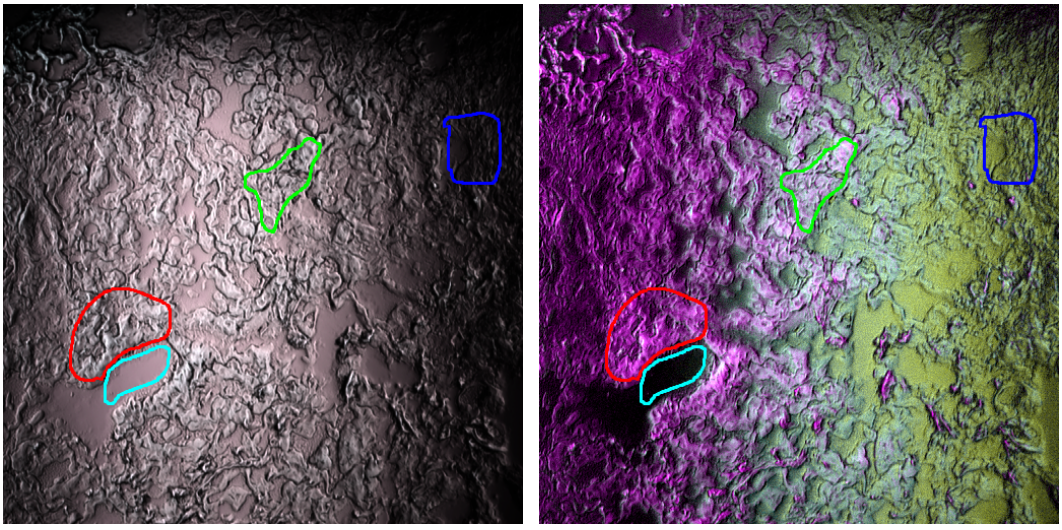

(a) Original CARS data.

(b) Processed CARS data

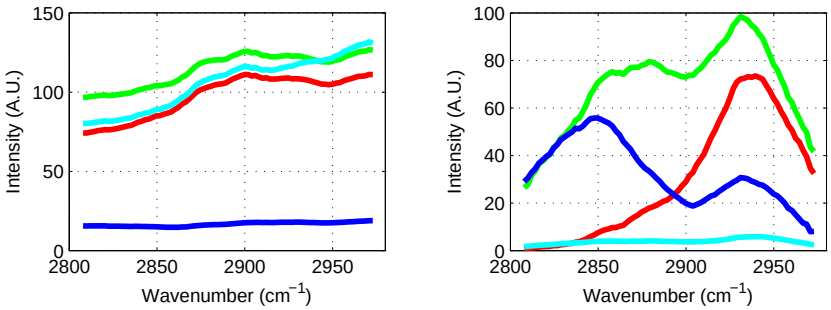

(c) Original spectra

(d) Processed spectra

Figure 8.14: Images of the tissue sample of the Calu-3 cell line. Images taken using a 85 mW signal beam and 100 mW fundamental beam, 3 Kalman averages and 12 µs pixel dwell time.

All following figures show measurements taken from the same sample that was later used for the DAPI and FISH imaging. Unless stated otherwise, these figures were created using a 90 mW signal beam and 100 mW fundamental beam with 2 Kalman averages and 22 µs pixel dwell time. One side of the image corresponds to 700 µm. The sample imaged is the 5th microscope slide of the set containing mouse tissue with a Calu-3 cell line human tumor.

Figure 8.15 shows a typical nice scan. The fat blobs are easily recognized - even in the unprocessed spectrum - by their strong resonances around 2850 and 2880 cm^{-1}. The rest of the sample appears to be mostly of the 'purple' type, with high protein and low fat signal. There are some deviating areas such as the green marked region which has more fat content than the rest of the purple tissue and some patches can be found that have very low protein contents. Based on the lipid and protein contents it could be suggested that most of the tissue visible here is cancer tissue, but considering the results from the FISH measurements we should rather consider this to be the normal ratio in healthy tissue, where cancer tissue would thus contain even more proteins and less lipids.

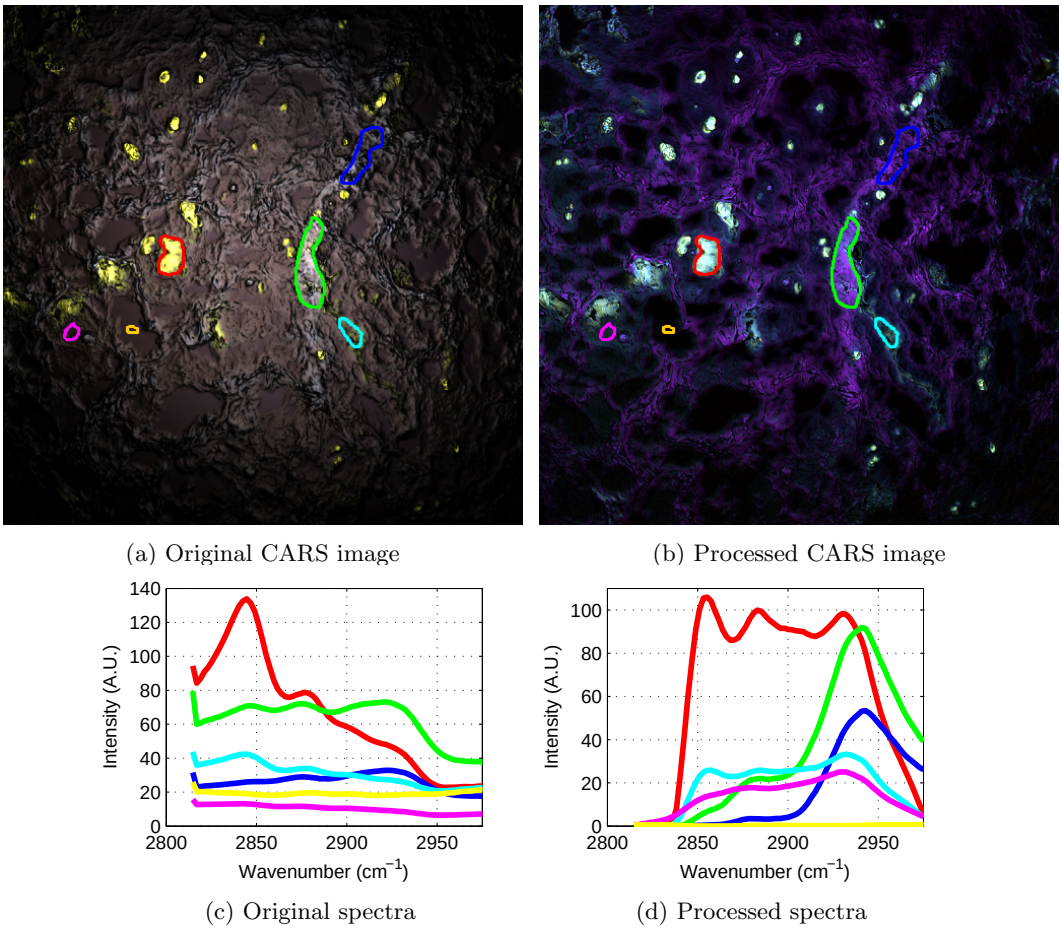

(a) Original CARS image

(b) Processed CARS image

(c) Original spectra

(d) Processed spectra

Figure 8.15: Measurement performed with 80 mW signal power. The fat blobs are already visible in the unprocessed data but more information is visible in the processed set.

In figure 8.16 a fat area can be seen in the lower left corner. It can easily be distinguished from the other fat areas within the tissue because it lacks the second lipid peak at 2880 cm^{-1}. This suggests it doesn't originate from the tissue itself but most likely is a contamination from outside. Other interesting features are the brighter area in the middle (blue and cyan ROI's) which appear to contain more lipids than the surrounding tissue. Similar tissue can be found around the edges of the sample, maybe forming a barrier between the environment and the tissue itself.

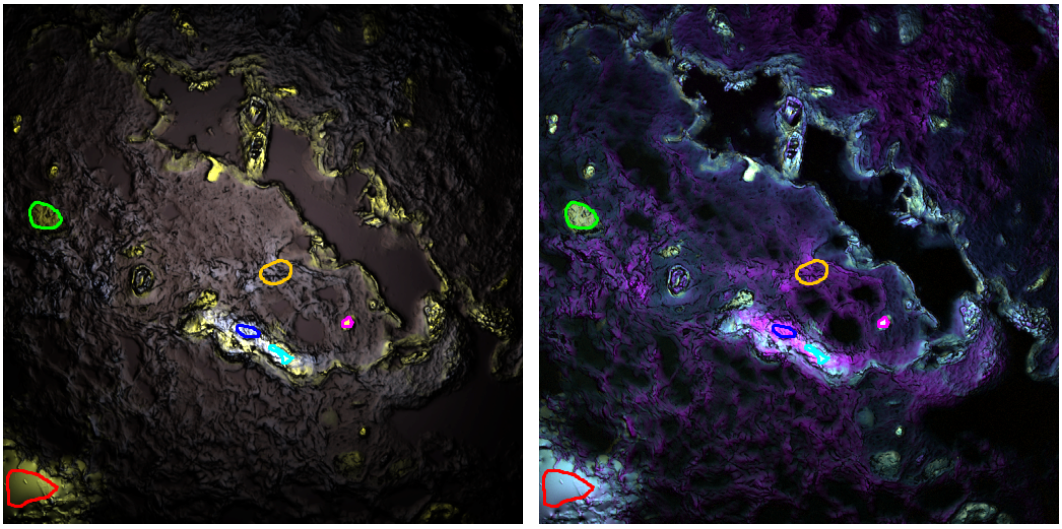

(a) Original CARS image

(b) Processed CARS image

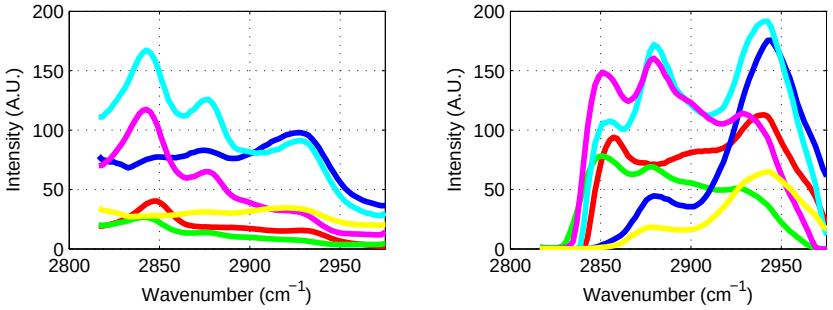

(c) Original spectra

(d) Processed spectra

Figure 8.16: The bright blob in the lower left corner is probably a contamination from outside. Other interesting areas are the lipid-rich edges of the tissue.

The tissue sample from figure 8.17 was potentially very useful due to the difference in morphology that is clearly visible. Unfortunately, it appears to be one of the more boring samples that were imaged, as can be seen in figure 8.17b and the corresponding spectra. There is a small area (cyan ROI) in the lower left corner causing a relatively strong lipid-related signal, but the rest of the tissue seems to be very similar to what was measured so far: high protein and low lipid signals. The green ROI circles the only area that resembles the lipid blobs from previous images. Due to the lower total signal strength it now appears slightly green.

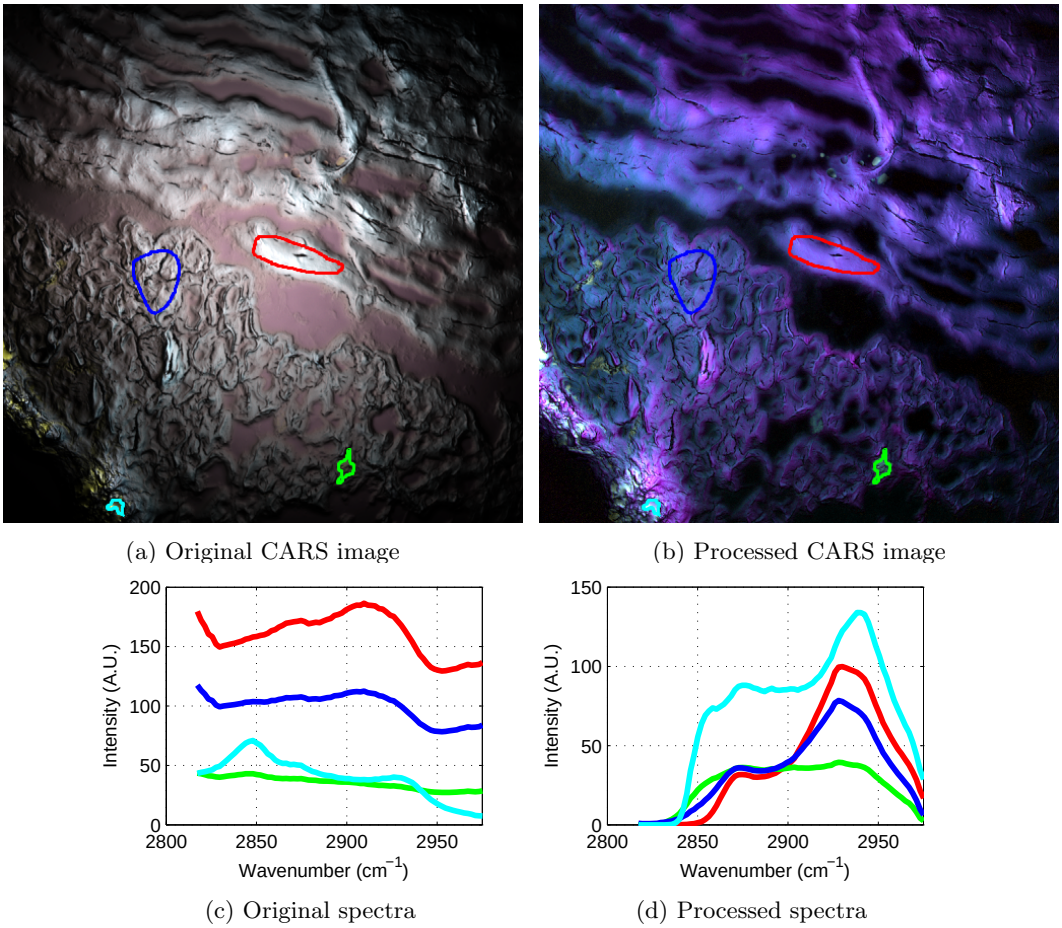

(a) Original CARS image

(b) Processed CARS image

(c) Original spectra

(d) Processed spectra

Figure 8.17: Originally thought to be very interesting due to the differences in morphology, but the spectra recorded show little variation.

In figure 8.18 one could argue about the presence of two types of tissue. The first type is similar to that what has been measured before: the purple tissue (blue ROI) with high protein and low lipid signal. This tissue shows up mostly in small thin strands with a lot of empty area in between. In the top part of the scan, this tissue appears to be a bit more firm. The second tissue type can be found in the bottom left, its spectrum is marked by the green ROI. Here, the relative fat content is much higher and this tissue appears much less 'broken' and looks more like a bulk. Again, the original thought was that the purple tissue was tumor tissue while the bulkier blue-grey tissue was healthy, based on the protein and lipid peaks. However, since the FISH measurement indicated none of these samples actually touched upon the tumor tissue there must be another explanation for the spectral difference.

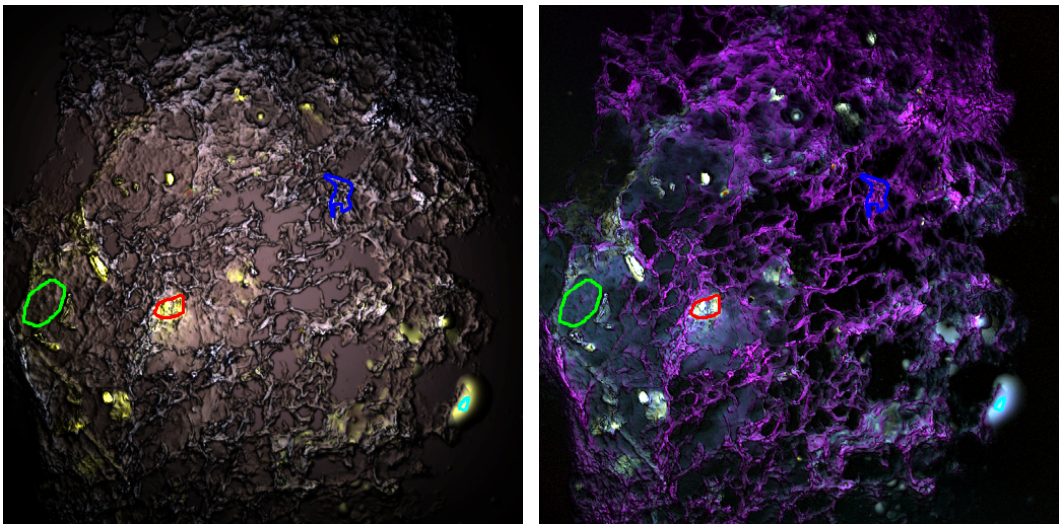

(a) Original CARS image

(b) Processed CARS image

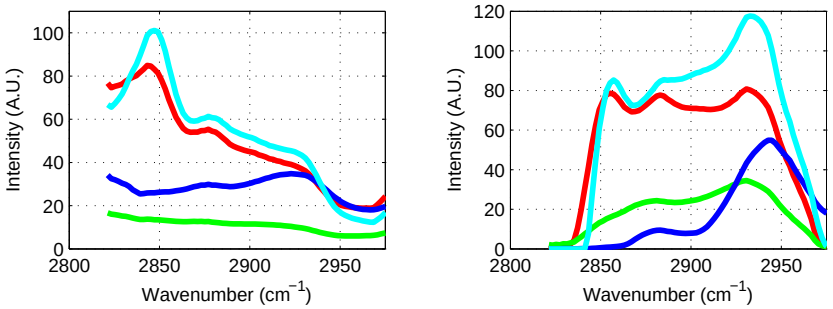

(c) Original spectra

(d) Processed spectra

Figure 8.18: Two main different types of tissue can be seen: the purple thin strands and the blue-grey tissue in the left part.

Figure 8.19 shows the final figure of this report. The most interesting feature is marked in the blue ROI. Where previously the only parts containing high lipid contents were the fat blobs themselves, here we can see one long strand that has many lipids too. The rest of the tissue remains as in the previous figure: high protein and low lipid signals with lots of open space in between.

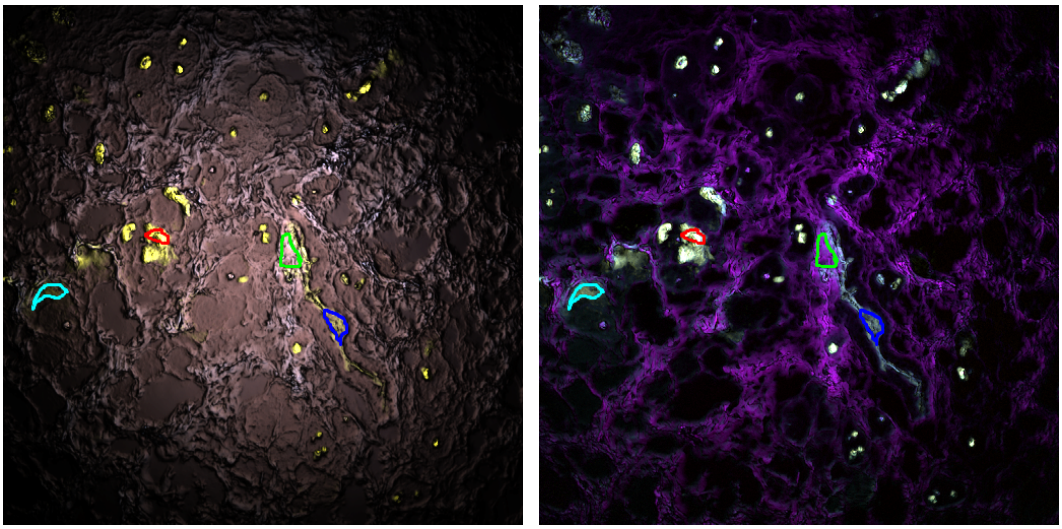

(a) Original CARS image

(b) Processed CARS image

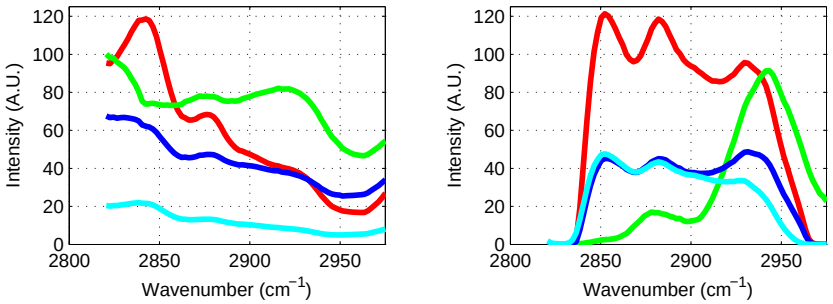

(c) Original spectra

(d) Processed spectra

Figure 8.19: Final image showing fat blobs within the regular tissue, but also some tissue strands containing more lipids than normal.

Chapter 9

Conclusion

The goal of this Master's project was to investigate the feasibility of using CARS microspectroscopy to distinguish between cancer tissue and healthy tissue. Preferably, the differences in spectra are detected in the fingerprint region of the vibrational resonances, where resonant peaks are more distinct and abundant than in the high wavenumber region where there are only a few. There were two main challenges to this goal. The first was the non-resonant background that is present in all CARS signals, but even more so in the fingerprint region. The second was the wide variety of differences between healthy tissue and the many different kinds of cancer spectra. During the project a third challenge presented itself: finding the border between healthy and cancer tissue in the samples. These locations were necessary in order to make comparisons between the different tissues within the same scan.

Through continuous improving of the processing algorithms used, the problem of a non-resonant background has been greatly reduced. Using a modified Kramers-Kronig algorithm to extract the phase of the signal in our spectra, we managed to transform the CARS signal into a signal that is nearly free from the non-resonant background. It strongly resembles measured SRS spectra, which again look very much like Raman spectra of which many are known for various tissues. Using two-sided padding and a singular value decomposition denoising algorithm the quality of these spectra was further improved. In the high wavenumber region, the resonant signal was strong enough to be effectively separated from the non-resonant background and noise. In the fingerprint region, however, the combination of (slightly) lower sensitivity of the CARS detectors with the significantly lower signal output of the samples resulted in the non-resonant background and other noise dominating the resonant signal so much that no useful extraction could be performed. This was the main reason for continuing the project in the high wavenumber region. It was also noticed that in some cases the non-resonant background was not equally removed from all corners of the image. While this could not be predicted by looking at the unprocessed data, re-alignment of the optical setup was successful in reducing this problem.

In many Raman-related tissue scans, either average spectra of complete samples are compared, or (colorcoded) images are created by extracting the main components of a spectrum and assigning a color to them, or by imaging at 3 vibrational resonances and creating an RGB composite image. Averaging the spectra of complete samples was no option here because of the imaging requirement. The other two options only use limited amounts of data which can result in false results when differences are subtle. Using our hyperspectral data the whole spectrum can be displayed for every pixel, creating color contrast where spectra differ. As a result, no prior knowledge about the spectrum is necessary. Due to the use of three look-up tables with one, two or three rainbow spectra different colored images are

created leaving the user to choose the image with most color contrast.

Altogether, the imaging of tissue using CARS in the high wavenumber region while using a Kramers-Kronig approach to remove the non-resonant background should be considered a success. Measurements in the fingerprint region remain a challenge for another time.

Despite our attempts, we have not been able to create images showing clear color contrast between healthy and cancer tissue. We are convinced that this is not due to the lack of resonant contrast, but rather due to the fact that we haven't been able to reliably locate such border regions to perform measurements on. Despite the successful identification of tumor tissue using DAPI staining and FISH, the differences between related samples were too large to use this knowledge for new guided measurements.

9.1 Outlook

Looking back at the project, a lot of things have been achieved. Still, there will always be things that remain to be done. In this case, one of the most useful follow-up steps would be measurements on a piece of tissue that is already confirmed to have both tumor tissue as well as healthy tissue. This will be the fastest way to prove that tissue differences can, indeed, clearly be shown in CARS measurements. Due to the lack of success in reliably predicting the location of healthy and tumor tissue from our side, it would be useful and easiest if preparation of those samples is done in close collaboration with the UMCG. One should then remember to use Cryomatrix instead of paraffin and samples should be placed on thin slides if the 60x water dipping objective is to be used.

A next logical step would be to expand the resonances to be probed to the fingerprint region. Although we were not (yet) able to extract useful information from this region, we are confident that when a higher SNR is reached spectral differentiation should work as expected. In order to increase the SNR, one should consider even longer integration times to further reduce the amount of noise. Also, thicker samples and microscope slides of CaF2 instead of normal glass will result in less (false) signal originating from the slide and more from the sample itself.

The current wide-field scans covering $\pm$ 170 wavenumbers take about 15 minutes to fully image an area of 700*700 µm. This is of course far too long to be ever used for in vivo measurements, where the scanned area should also be much larger. During this project however, we have focused on image quality rather than speed. As such, one could drastically reduce the resolution and scanning time per pixel, resulting in a much faster acquisition time. The quality of the resulting images will obviously decrease, but in that phase of the research it should be relatively easy to find the fastest scan time where crucial spectral differences can still be resolved. Although a possible application is still far into the future, one could think about designing a small probe that can roughly image a small area within a minute. Performing multiple of those measurements on spots that look 'interesting' from an oncologist's point of view could then relatively fast give an indication of the tissue being probed. For the direct future however, improvement in the fingerprint regime as well as verification of the color contrast should take priority. In the meantime, high-resolution scans could still be used for analysis of ex vivo samples.

Chapter 10

Acknowledgements

This thesis is not only the end of my Master's assignment, but also marks the end of five and a half great years of being a student. These years have not been spent alone and therefore I'd like to use this opportunity to thank the many people who have made my time in Enschede the adventure that it was.

The first people to be mentioned are my flatmates from Calslaan 13-1. Over the years I've seen nearly every room in our flat change its owner and with all those people I've had great experiences. A ski trip to France, a holiday to Poland, random barbecues or midnight bonfires, blocking our neighbor's door with snow and ice, pranking each other with cups of water on the floor, Christmas dinners and Sinterklaas evenings, re-naming the flat to "The Turned Table" or "Triple T", painting Pikachu, Mario and Rafiki on the walls, there's so much to remember. I thank you all for a great time!

The next group I'd like to thank is my friends from Applied Physics (both Bachelor and Master) and my study association, S.V. Arago. Having heard different stories about different study associations I figured I'd join Arago, buy their cheaper study books and then just see what happens. Little did I know that I would spend many of my lunch breaks in the Arago Kamer, reading Donald Duckjes, grabbing candy from the cabinet and relaxing on the couches with friends. I soon joined Objectief in order to take photographs of events organized by Arago and later even joined the study tour committee Shoshin that would organize an awesome trip to Japan. All these experiences have broadened my perspective a lot, for which I'm very grateful!

Spending many hours on physics could sometimes be quite challenging, so I needed a hobby to catch some fresh air and get rid of excess energy. I found one - Parkour - and with it came more friends. I joined the group somewhere during my first year thinking "Oh, that sounds cool, I want to do that too!". I will never forget the days after my first training, shuffling my way around the university because of the massive muscle aches. Things got better very fast though, and over the years Parkour has taught me to explore and expand my limits. Apart from the sportive aspect, the Parkour group is a great group of friends with whom we could have lots of fun, regardless of the setting. The fact that I have been banned from suggesting any funny songs will probably say enough!

Having arrived at the Master's phase of my education, I spent more and more time at Optical Sciences. Its informal setting, approachable staff members and likewise minded members made it into a group I enjoyed being with every day. I have fond memories of testing a new speaker setup in Carré during "beer-o-clock", a retreat to Belgium, the Thorlabs

challenge, Nerf guns and RC helicopter dogfights in our office, the amount of posters behind Seans desk that kept increasing and much more. You all are a great bunch of people!

If - for some reason - years of studying haven't made you realize this until now, a Master's thesis once more confirms that research is not done all by yourself! This thesis is no different from all the others. I have had a lot of help from many people from different places, and would like to thank all of them. Let me start by thanking Herman Offerhaus who was my supervisor during my thesis. We've discussed ideas, tinkered with the setup together and he's given me valuable ideas and tips while leaving the exact direction in which I was heading very open. Rick Krabbendam, my PhD supervisor, often had different obligations but would still help me out whenever I needed his help. Erik Garbacik - who worked at OS on the same setup as me but now works in Barcelona - has provided me with invaluable information over the email. When I wasn't sure of the possibility of something or needed help figuring out a problem, he'd do his best to help me as well as he could. Jeroen Korterik and Frans Segerink, the technicians of the group, were always available for (technical) advice. Hop by their office for a brief questions, and you'll be talking about the newest laser for 10 minutes before you know it!

Not only within OS there was a lot of help. Jolien Tjalma, Arjan Kol and Martin Pool from the UMCG provided me with samples, varying from pre-cut coupes to a complete mouse leg with tumor attached, frozen in a plastic tube. Shaun Burer and Parthiban Periyasami from the Developmental BioEngineering group at the University of Twente have kindly helped cryosectioning the samples. Furthermore, Niels van der Velde and Joost van Swennenhuis from Medical Cell BioPhysics have been a great help by performing the DAPI and FISH measurements for me, providing me with extra information on the samples.

Making a last jump back to my friends, I'd like to thank Martin and Jenneke. Having met at the Junior College Utrecht in the 5th year of secondary school, we soon parted ways again when we started our studies, although Martin joined the University of Twente as well. Over the last few years, we haven't had regular contact, but whenever we did meet up or talk it'd be like we'd seen each other just the day before. Thank you for a great friendship, I hope to maintain it indefinitely!

By now, there's just one group left to thank: My family. Without my parents and my sister, I would not have made it this far. They have fed my curiosity from a very young age and made sure to guide me towards becoming the person I am today. On some days this would mean urging me to start studying because my planning skills were dreadfully absent, on others it would mean telling me to take a break or have some fun because I really, really had studied enough for that exam. Dad, mom, sis:

Thank you for everything!

Chapter 11

Bibliography

[1] Centraal Bureau voor de Statistiek, StatLine Database. Accessed February 2015. http://statline.cbs.nl/Statweb/publication/?DM=SLNL&PA=7052_95&D1=0,7-29,42-48&D2=0&D3=0&D4=62-63&HDR=G1,G2,G3&STB=T&VW=T

[2] American Cancer Society. "How is bone cancer diagnosed?" Accessed February 2015. http://www.cancer.org/cancer/bonecancer/detailedguide/bone-cancer-diagnosis

[3] G.M. van Dam, G. Themelis, L.M.A. Crane, N.J. Harlaar, R.G. Pleijhuis, W. Kelder, A. Sarantopoulos, J.S. de Jong, H.J.G. Arts, A.G.J. van der Zee, J. Bart, P.S. Low, V. Ntziachristos. "Intraoperative tumor-specific fluorescence imaging in ovarian cancer by folate receptor-α targeting: first in-human results." *Nature Medicine* **17**, pp. 1315-1319, 2011. http://www.nature.com/nm/journal/v17/n10/full/nm.2472.html

[4] American Cancer Society. "Do x-rays and gamma rays cause cancer?" Accessed February 2015. http://www.cancer.org/cancer/cancercauses/radiationexposureandcancer/xraysgammaraysandcancerrisk/x-rays-gamma-rays-and-cancer-risk-do-xrays-and-gamma-rays-cause-cancer

[5] C.V. Raman, K.S. Krishnan. "A new type of secondary radiation." *Nature* **121**, pp. 501-502, 1928.

[6] E. Smith, G. Dent. *Modern Raman Spectroscopy - A Practical Approach.* John Wiley & Sons Ltd , 2005.

[7] A. Smekal. "Zur Quantentheorie der Dispersion." *Naturwissenschaften*, Volume **11**, Issue 43, pp. 873-875, 26. Oktober 1923.

[8] G.J. Thomas, Jr. "Raman Spectroscopy of Protein and Nucleic Acid Assemblies" *Annual Review of Biophysics and Biomolecular Structure.* **28**:1-27, 1999.

[9] B. Huang, Y. Tian, Z. Li, S. Gao, Z. Li. "Temperature measurement from the intensity ratio of the Raman-scattering lines in carbon tetrachloride constituting the liquid core of an optical fiber." *Instruments and Experimental Techniques*, Volume **50**, Issue 2, pp. 282-285, March 2007.

[10] TSI. "Gas Phase Process Raman Analyzers." Accessed February 2015. http://www.tsi.com/gas-phase-process-raman-analyzers/

[11] L.M. Malard, M.A. Pimenta, G. Dresselhaus, M.S. Dresselhaus, "Raman spectroscopy in graphene." *Physics Reports*, Volume **473**, Issues 5–6, pp. 51–87, April 2009.

[12] K. Maquelin, L.P. Choo-Smith., H.P. Endtz, H.A. Bruining, G.J. Puppels, "Rapid Identification of Candida Species by Confocal Raman Microspectroscopy." *Journal of Clinical Microbiology,* Volume **40** no.2, pp. 594-600, February 2002.

[13] M. Pérez-Alonso, K. Castro, J. M. Madariaga. "Investigation of degradation mechanisms by portable Raman spectroscopy and thermodynamic speciation: The wall painting of Santa María de Lemoniz (Basque Country, North of Spain)" *Analytica Chimica Acta.* Volume **571**, Issue 1, pp. 121-128, 30 June 2006.

[14] Siddhartha Mukherjee. *The Emperor of All Maladies: A Biography of Cancer.*

[15] J. Surmacki, J. Musial, R. Kordek, H. Abramczyk "Raman imaging at biological interfaces: applications in breast cancer diagnosis", *Molecular Cancer*, **12**:48, 2013.

[16] Z. Huang, A. McWilliams, H. Lui, D.I. McLean, S. Lam, H. Zeng, "Near-Infrared Raman Spectroscopy for Optical Diagnosis of Lung Cancer", *International Journal of Cancer*, volume **107**, pp. 1047-1052, 2003.

[17] U. Utzinger, D.L. Heintzelman, A. Mahadevan-Jansen, A. Malpica, M. Follen, R. Richards-Kortum, "Near-Infrared Raman Spectroscopy for in Vivo Detection of Cervical Precancers" *Applied Spectroscopy*, Volume **55**, Number 8, pp. 955-959, 2001.

[18] C.M. Krishna, N.B. Prathima, R. Malini, B.M. vadhiraja, R.A. Bhatt, D.J. Fernandes, P. Kushtagi, M.S. Vidyasagar, V.B. Kartha, "Raman spectroscopy studies for diagnosis of cancers in human uterine cervix", *Vibrational Spectroscopy*, Volume **41**, pp. 136-141, 2006.

[19] K. Maheedhar, R.A. Bhat, R.Malini, N.B. Prathima, P. Keerthi, P. Kushtagi, C. Murali Krishna, "Diagnosis of Ovarian Cancer by Raman Spectroscopy: A Pilot Study" *Photomedicine and Laser Surgery.* Volume **26**, Number 2, pp. 83-90, 2008.

[20] S. Kennedy, "Formalin Fixed Paraffin Embedded Tissue DNA Isolation: The Basics" Mo Bio Laboratories, Inc. Accessed February 2015. `http://www.mobio.com/blog/2012/07/20/formalin-fixed-paraffin-embedded-tissue-dna-isolation-the-basics/`

[21] M. Gniadecka, O.F. Nielsen, D.H. Christensen, H.C. Wulf. "Structure of Water, Proteins, and Lipids in Intact Human Skin, Hair, and Nail" *Journal of Investigative Dermatology* **110**, 393-398, 1998. `http://www.nature.com/jid/journal/v110/n4/full/5600034a.html`

[22] A. van Rhijn. "Tailoring Pulses for Coherent Raman Microscopy", PhD thesis at the University of Twente, 2012.

[23] Xie Group. "Stimulated Raman Scattering Microsopy". Accessed February 2015 `http://bernstein.harvard.edu/research/SRS.htm`

[24] E.O. Faoláin, M.B. Hunter, J.M. Byrne, P. Kelehan, H.A. Lambkin, H.J. Byrne, F.M. Lyng, "Raman Spectroscopic Evaluation of Efficacy of current Paraffin Wax Section Dewaxing Agents", *Journal of Histochemistry & Cytochemistry.* Volume 53(1): 121-129, 2005.

[25] A. Kunstar, "Confocal Raman Microspectroscopy - Applications in Cartilage Tissue Engineering", PhD Thesis at the University of Twente, 2012. `http://www.utwente.nl/tnw/dbe/publications/Dissertations%20files%20of%20Graduates/Kunstar%20-%20Confocal%20Raman%20Microspectroscopy%20Applications%20in%20Cartilage%20Tissue%20Engineering%20-%202012/PDF.pdf`

[26] F. Masia, A. Glen, P. Stephens, P. Borri, W. Langbein, "Quantitative Chemical Imaging and Unsupervised Analysis Using Hyperspectral Coherent Anti-Stokes Raman Scattering Microscopy", *Analytical Chemistry*, Volume **85**, pp. 10820-10828, 2013.

[27] R. Galli, V. Sablinskas, D. Dasevicius, A. Laurinavicius, F. Jankevicius, E. Koch, G. Steiner, "Non-linear optical microscopy of Kidney Tumors" *Journal of Biophotonics*, Volume **7**, No. 1-2, pp. 23-27, 2014.

[28] M. Jurna, E.T. Garbacik, J.P. Korterik, J.L. Herek, C. Otto, H.L. Offerhaus, "Visualizing resonances in the complex plane with vibrational phase contrast CARS", *Analytical Chemistry*, vol. **18**, pp. 046009-1-5, 2013.

[29] H.A. Rinia, M.B. Bonn, M. Müller, E.M. Vartiainen, "Quantitative CARS Spectroscopy Using the Maximum Entropy Method: The Main Lipid Phase Transition", *ChemPhysChem*, Volume 8(2), 279-287, 2007.

[30] Y. Liu, Y.J. Lee, M.T. Cicerone, "Broadband CARS spectral phase retrieval using a time-domain Kramers-Kronig transform", *Optics Letters*, Vol. **34**, No. 9, pp. 1363-1365, 2009.

Chapter 12

Appendix

```
%% Performs Kramers-Kronig processing on a datastack (X,Y, lambda)
% in order to extract the phase and then remove the NRB to retrieve the
% Raman spectrum. Application of the singular value decomposition, the
% Kramers-Kronig processing, spectral- and spatial power correction and
% creation of the final .tiff file can be turned on and off. A minimum and
% maximum frame number (related to wavenumber) must be given in order to
% only use data that does not contain strong jumps in the wavenumbers
% probed.
close all
clear all;
clc

%% Desired Manual Inputs
SVD=1;          %1 for Singular Value Decomposition, 0 for NO SVD.
createTIF=1;    %1 for creating a TIF, 0 for not doing so.
specpowcorr=1;  %0=off, 1=CARS (squared), 2=SRS (linear)
PROCES=1;       %1 for processing, 0 for no processing.

savefolder='C:\Users\Sven vB\Documents\Matlab\';
filenametif='combi1_x123y312_test.tif';     %Filename for exported file

% Image size, possibility to take a crop of the image
xmin=1;
xmax=512;
ymin=1;
ymax=512;

% Define pixel with almost only nonresonant background signal.
% NOTE: When using imshow and selecting a pixel, matlab will say X=25,Y=40. This
% corresponds to the datapoint stack(40,25), so stack(Y,X), not intuitive!
% Below, enter the (intuitive) X and Y coordinate of the image.
XnrX=123;
XnrY=312;

%% Loading actual data.
% The script master_read_fluoview uses automatic_directory_read which in
% turn uses read_fluoview and rd_img16. These four scripts have been
% created by Rick Krabbendam at the Optical Sciences group to import
% Fluoview multi-page .tiff files into matlab.
master_read_fluoview;
cd (b)
origfilename=names_files(2,5:end);  %Extract file name
pars=load(origfilename);            %Loads wavenumbers & power info
w=pars(:,2);                        %Wavenumbers
P=pars(:,3);                        %Power info
```

```
46
47  % Check for and remove any unexpected large jumps in wavenumber by cropping
48  % the data:
49  find(diff(w)<0)
50  f=figure(1);
51  subplot(2,2,1)
52  plot(diff(w))
53  title('Diff(w)')
54  hold on
55  subplot(2,2,2)
56  plot(P,'r')
57  title('Power')
58  subplot(2,2,3)
59  plot(w,'g')
60  title('Wavenumber')
61
62  % Select the channel to extract data from. These relate to the three
63  % channels in Fluoview.
64  splitfile=input('Select 1st, 2nd or 3rd channel (if available)?\n')
65  if splitfile==1
66      stack=double(data.(['ch1e' origfilename]));
67  elseif splitfile==2
68      stack=double(data.(['ch2e' origfilename]));
69  elseif splitfile==3
70      stack=double(data.(['ch3e' origfilename]));
71  end
72
73  % Crop data if desired.
74  firstframe=input('What is the lower border?\n');
75  lastframe=input('What is the upper border?\n');
76  w=w(firstframe:lastframe);
77  P=P(firstframe:lastframe);
78  close(f)
79
80  wmin=min(w);
81  wmax=max(w);
82  % Add just a little bit to all data points, to prevent all 0-values from
83  % wreaking havoc in the calculation of the natural logarithms, Fourier
84  % transforms and Uint_16 conversion.
85  stack=stack(:,:,firstframe:lastframe)+0.000000001;
86  clear data
87
88  cd 'C:\Users\Sven vB\Documents\Measurements\'
89
90  %% Power correction (spectral)
91  tic
92  power(1,1,:)=P;
93  power=repmat(power,xmax-xmin+1,ymax-ymin+1);
94  if specpowcorr==1
95      stack=stack./(power.^2);
96  elseif specpowcorr==2
97      stack=stack./power;
98  end
99  disp('Spectral power correction applied')
100 toc
101
102 clear power
103
104 %% Perform SVD and remove noise
105 tic
106 if SVD==1
107     new=zeros(size(stack,1)*size(stack,2),size(stack,3));
108     for x=xmin:xmax
109         for y=ymin:ymax
110             i=(x-1)*xmax+y;
111             new(i,:)=stack(x,y,:);
```

```
        end
    end

    [U,S,V]=svd(squeeze(sqrt(new)),0);

    % Do linear fit for last 50% of datapoints
    xforfit=1:size(stack,3);
    yforfit=diag(S).';
    begin=floor(length(xforfit)/2);
    p=polyfit(xforfit(begin:end),yforfit(begin:end),1);
    yfit=polyval(p,xforfit);

    % Remove points for which the singular value is NOT larger than sqrt(2)
    % times the fit
    Sf=S;
    for i=1:size(stack,3)
        if Sf(i,i)<sqrt(2)*yfit(i)
            Sf(i,i)=0;
        end
    end
    new=U*Sf*V';

    for x=xmin:xmax
        for y=ymin:ymax
            i=(x-1)*xmax+y;
            stack(x,y,:)=new(i,:);
        end
    end

    stack=stack.^2;

end
clear U S V
display('SVDs calculated & noise reduced')
toc

%%
if PROCES==1
    %% Interpolate data
    tic
    H=waitbar(0,'Interpolating spectra');
    w_intpol=linspace(wmin,wmax,length(w))';
    stack_intpol=zeros(xmax-xmin,ymax-ymin,length(w));
    for x=xmin:xmax
        for y=ymin:ymax
            stack_intpol(x,y,:)=interp1(w,squeeze(stack(x,y,:)),w_intpol);
        end
        waitbar((x-xmin)/(xmax-xmin))
    end
    w_old=w;
    w=w_intpol;
    stack=stack_intpol;
    clear stack_intpol w_intpol
    disp('w interpolated')
    toc
    delete(H)

    %% Padding procedure
    tic
    H=waitbar(0,'Padding spectra');
    newstack=zeros(xmax-xmin+1,ymax-ymin+1,3*size(stack,3))+0.000000001;
    steps=length(w);
    newstack(:,:,steps+1:2*steps)=stack;
    stack=newstack;
    clear newstack
    for x=xmin:xmax
```

```
178             for y=ymin:ymax
179                 stack(x,y,1:steps)=stack(x,y,steps+1);
180                 stack(x,y,2*steps+1:end)=stack(x,y,2*steps);
181             end
182             waitbar((x-xmin)/(xmax-xmin))
183         end
184         delete(H)
185         disp('Data has been padded')
186         toc
187 
188         wd=(max(w)-min(w))/(steps-1);
189         w=linspace(min(w)-(steps*wd),max(w)+(steps*wd),3*steps);
190 
191         %% Taking most likely Xnr-spectrum, averaged over a 3x3 pixel area.
192         for i=1:3
193             for k=1:3
194                 tmp(i,k,:)=stack(XnrY+i-1,XnrX+k-1,:);
195             end
196         end
197         tmp=mean(tmp,1);
198         tmp=mean(tmp,2);
199         Xnr=sqrt(tmp);
200 
201         %% Processing spectrum
202         tic
203         stackproc=zeros(size(stack,1),size(stack,2),size(stack,3));
204         H=waitbar(0,'Computing spectra');
205         phi=zeros(xmax-xmin+1,ymax-ymin+1,length(w));
206         Z=zeros(1,length(w));
207 
208         %inverse fourier transform on Xnr signal
209         invXnr=ifft(log(abs(Xnr)));
210 
211         for x=xmin:xmax
212             for y=ymin:ymax
213                 X=sqrt(squeeze(stack(x,y,:)));
214 
215                 %inverse fourier transform on X signal
216                 invX=ifft(log(abs(X)));
217 
218                 %Replacing left part with Xnr instead of X
219                 combined=invX;
220                 for i=ceil(length(X)/2):length(X)
221                     combined(i)=invXnr(i);
222                 end
223 
224                 reproX=fft(combined);
225 
226                 phi(x,y,:)=2*imag(reproX(1:length(X))-log(abs(X))/2);
227 
228                 stackproc(x,y,:)=abs(X).*sin(squeeze(phi(x,y,:)))*-1;
229             end
230             waitbar((x-xmin)/(xmax-xmin))
231         end
232         delete(H)
233         clear stack
234 
235         res=stackproc(xmin:xmax,ymin:ymax,:);
236         clear stackproc phi
237 
238         %Normalizing for tiff file saving.
239         res=uint16(res*(2^12/max(res(:))));
240         disp('Processing finished')
241         toc
242     else
243         res=uint16(stack*(2^12/max(stack(:))));
```

```
244 end
245
246 %% Creating TIFF file
247 if createTIF==1;
248     tic
249     cd(savefolder)
250     t = Tiff(filenametif,'w');
251
252     tagstruct.ImageLength = size(res,1);
253     tagstruct.ImageWidth = size(res,2);
254     tagstruct.Compression = 1;  %Tiff.Compression.None
255     tagstruct.SampleFormat = 1; %Tiff.SampleFormat.Uint ofzo
256     tagstruct.Photometric = Tiff.Photometric.MinIsBlack;
257     tagstruct.BitsPerSample = 16;
258     tagstruct.SamplesPerPixel = 1;
259     tagstruct.PlanarConfiguration = Tiff.PlanarConfiguration.Chunky;
260     tagstruct.Software = 'MATLAB';
261
262     %Set tags.
263     t.setTag(tagstruct)
264
265     %Write first image
266     H=waitbar(0,'Writing to TIFF');
267
268     if PROCES==1
269         t.write(res(:,:,steps+1))
270         for i=steps+2:2*steps
271             t.writeDirectory;
272             t.setTag(tagstruct);
273             t.write(res(:,:,i));
274             waitbar((i/(size(res,3))))
275             wforsave=w(steps+1:2*steps);
276         end
277         save('w.txt','wforsave','-ascii')
278     elseif PROCES==0
279         t.write(res(:,:,1))
280         for i=2:size(res,3)
281             t.writeDirectory;
282             t.setTag(tagstruct);
283             t.write(res(:,:,i));
284             waitbar((i/(size(res,3))))
285         end
286     end
287
288     %Close tiff container
289     t.close();
290     delete(H)
291 else
292 end
293 disp('TIF saved')
294 toc
```

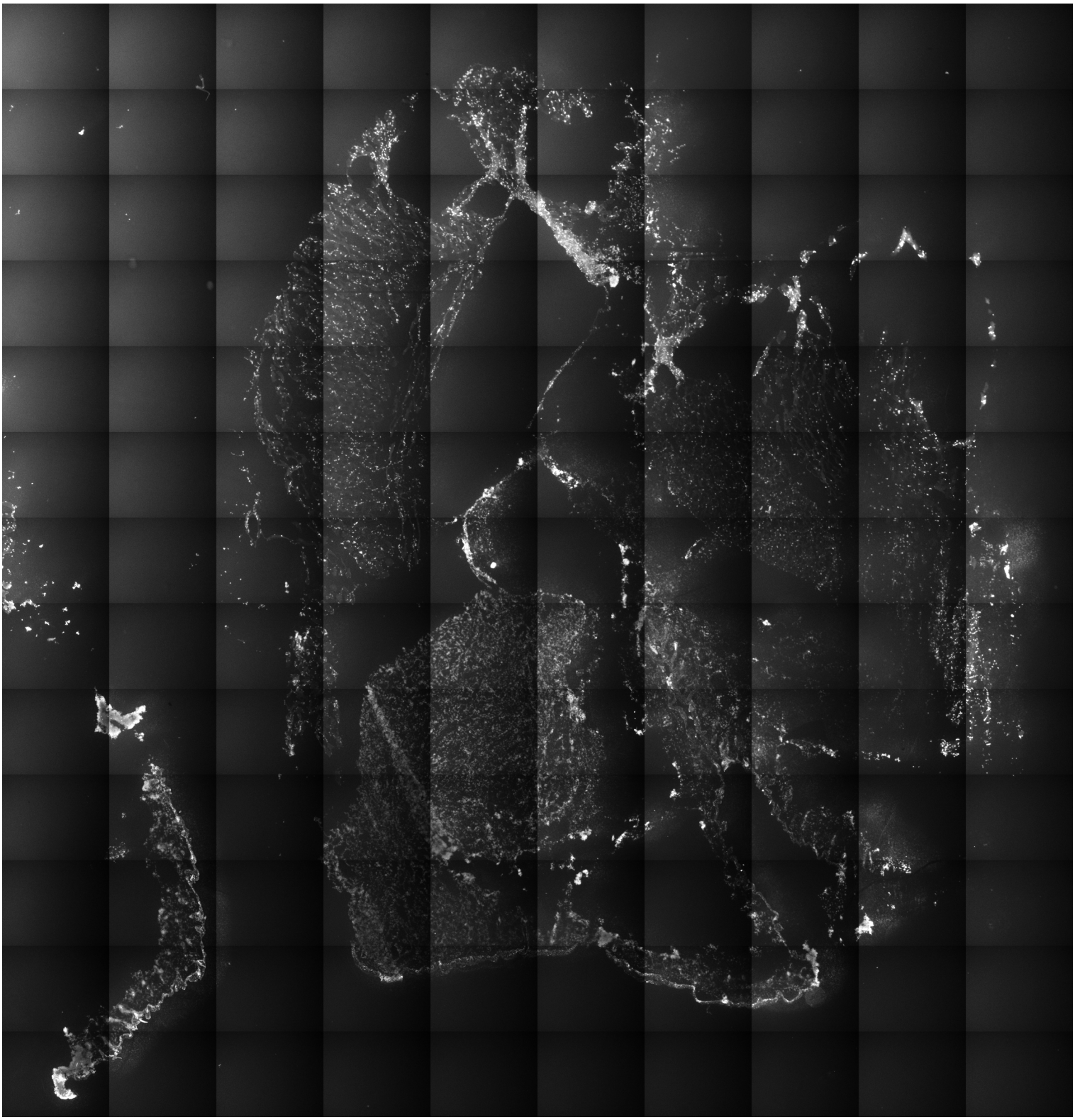

Figure 12.1: Full-page version of figure 8.12

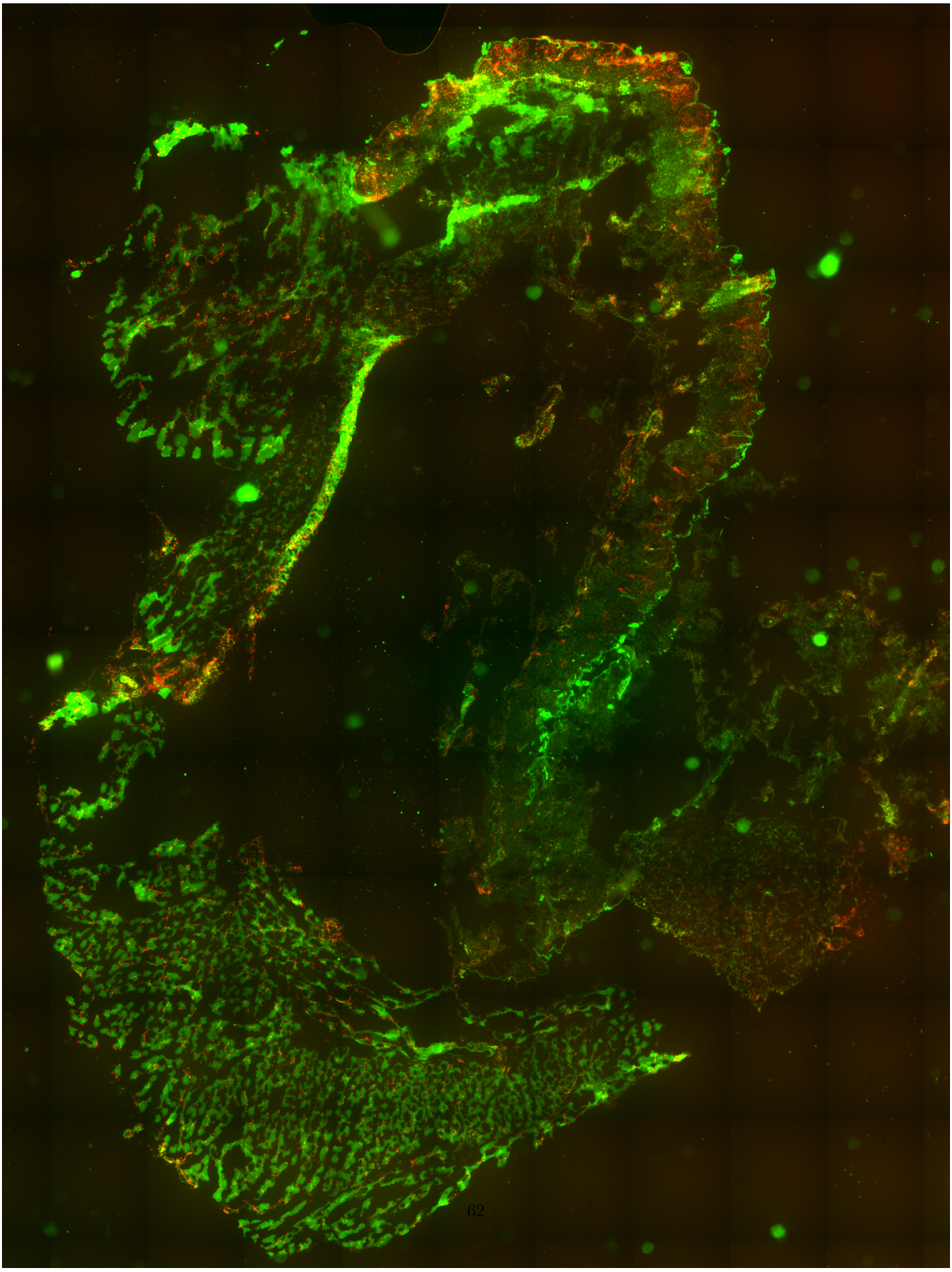

Figure 12.2: Full-page version of figure 8.13